Dielectric Metasurface Designs for Surface Enhanced Raman Scattering with Large Distances between Nanoparticles

by

Jeroen Dekker

A Master's Thesis

Company supervisor: Prof. Dr. G. Gerini TU Delft supervisor: Prof. Dr. B. Rieger

Date of Defense: Juli 12, 2023

A thesis submitted for the master's degree Biomedical Engineering

Abstract

In this thesis new dielectric metasurfaces in immersion were explored with a periodic distribution of unit cells with multiple silicon cylinder structures on a reflective gold slab with a fused quartz spacer in between. These new metasurfaces were designed with 60 nm and 130nm gaps in order to improve manufacturability and enable larger particles to enter the hotspot region while trying to maintain high electric field enhancement and enhancement factors. This was done by simulating the plane wave excitation in a range of 750 nm to 850 nm for a large number of metasurfaces using electromagnetic modelling software Lumerical using its finite difference time domain method. After exploring multiple silicon cylinder structures the focus was put on periodic metasurfaces with unit cells containing single, dimer, and quadrumer positioning of cylinders and enhancement factors of between 500-2000 were found. Afterwards the found fields for new promising designs were used in an optical trapping algorithm were enhancement factors for 10 nm particles were found between 10⁴-10⁵ and for 40 nm particles between 10³-10⁴. The effect of exciting a metasurface with circular polarization for quadrumer structures was thoroughly investigated but yielded no better enhancement factor than previous dimer designs. A new optical trapping scheme where the laser intensity is increased near the end of optical trapping is proposed to give slight improvement of enhancement factors after trapping. Overall, the limitations of the electromagnetic simulations and optical trapping algorithm makes it difficult to assume the enhancement factors found are realisable in experiment. These limitations need to be addressed before any conclusions can be made on whether immersion SERS offers any advantages over dry SERS in the case of dielectric metasurfaces.

Contents

L	List of Abbreviations				
П	List of Symbols				
1	Introduction				
2	Theory				
	2.1 Fundamentals				
	2.1.1 Raman scattering				
	2.1.2 Mie resonances				
	2.1.3 Enhancement Factor				
	2.2 SERS				
	2.2.1 Plasmonics				
	2.2.2 Localized Surface Plasmon resonances				
	2.2.3 Dielectric SERS				
	2.2.4 Surface lattice resonances				
	2.3 EFs of hotspots found in metasurfaces				
	2.3.1 SERS hotspots				
	2.3.2 Enhancement fields by dielectric metasurfaces				
	· · · · · · · · · · · · · · · · · · ·				
	2.4 Finite Difference Time Domain method				
	2.5 Optical trapping				
	2.5.1 Dielectrophoresis				
	2.5.2 Optical trapping in SERS				
	Method				
	3.1 Reproduction and Convergence testing				
	3.2 Exploration and optimization				
	3.3 Optical trapping with new Designs				
	or operation trapping with new 2 colons of the trapping with new 2 colors of the trapping with new 2 colons				
	Results				
	4.1 Multiple cylindrical structures				
	4.1.1 Linear vs circular polarization				
	4.1.2 Dimer vs quadrumer				
	4.2 Trapping schemes				
	4.3 Line metasurface				
	Discussion				
	Conclusion				
	Appendices				
	A Literature research				
	B Convergence test				
	C Reproduction Cameron				
	D Lumerical settings				
	E Additional results multiple structures				
	F Variable structure parameters metasurfaces				
	G Comparison of trapping distributions between various metasurfaces				

I List of Abbreviations

Abbreviation	Meaning	Page
CDA	Coupled Dipole Approximation	11
CT	Charge Transfer	9
ED	Electric Dipole	9
EF	Enhancement field	1
EM	Electromagnetic	2
FEM	Finite Element Method	18
FDTD	Finite Difference Time Domain	8
LSP	Localized Surface Plasmon	6
LSPR	Localized Surface Plasmon Resonance	7
MD	Magnetic Dipole	9
ME	Maximum Electric field	19
NH	Nano Hole	14
NIR	Near InfraRed	6
NP	Nano Particle	4
PML	Perfectly Matched Layers	15
RS	Raman Spectroscopy	1
SERS	Surface Enhanced Raman Spectroscopy	1
SLR	Surface Lattice Resonance	10
SM-SERS	Single Molecule Surface Enhanced Raman Spectroscopy	13
SP	Surface Plasmon	6
SPP	Surface Plasmon Polariton	6
TE	Transverse Electric	4
TM	Transverse Magnetic	4
UV	Ultra Violet	6
VIS	VIsible Spectrum	6

II List of Symbols

Symbol	Meaning	Page
A	Vector potential	4
B	Magnetic flux density	4
b	Impact parameter for light ray on sphere	4
C_{ext}	Extinction crosssection of coupled dipoles	11
c	Speed of light	4
D_i	Length of direction i of unitcell of periodic metasurface	10
d_p	Diameter of analyte particle	22
$oldsymbol{E}$	Electric field	3
E_0	Electric field amplitude of incident plane wave	11
F	Force	16
H	Magnetic field	14
h_c	Height of cylinder	21
$h_l^{(1)}$	Spherical Hankel function of the first order for the lth mode	4
$I^{'}$	Raman Scattering intensity	1
\boldsymbol{j}_f	Free current	15
j_i	Spherical Bessel functions of the first order for the lth mode	4
\vec{k}	Wave number	4
k_b	Boltzmann constant	16
L_E	LE the energy losses per cycle in resonator	7
l	the nth mode of the wave function solutions for TE and TM spherical waves	4
M_{loc}, M_{rad}	Local and radiative enhancement factor	5
m, p	The diffracted order of grating resonance of square grating	10
N	Average number of molecules in the scattering volume	1
n	Refractive index of nano particle	4
P_l^1	The associated Legendre polynomials of the first kind	4
$ {P}$	Polarization of multiple coupled dipoles	11
$oldsymbol{p}$	Dipole moment	3
Q	Quality factor	7
q_k	Normal mode coordinate	3
R	Radius of homogeneous sphere	4
r	Position vector	4
r_c	Radius of cylinder	21
r_{TE}, r_{TM}	Reflection coefficients of TE and TM reflected waves	16
S	Unitcell surface of the simulated metasurface	6
S_{dip}	The retarded dipole sum of multiple dipoles	11
S_E	The energy stored per cycle in resonator	7
[S]	PML tensor	16
s	Size parameter for the Mie resonance	9
T	Temperature of immersion fluid	16
t	Time	4
u,w	Wave functions of TE and TM spherical waves respectively	4
v_l	Frequency of radiation incident on analyte	3
v_m	Frequency matching with energy difference of vibrational modes	3
v_s, v_{as}	Stokes and anti-Stokes radiation scattered from analyte	3
V	Unitcell volume of the free space in the simulated metasurface	6
x	length of simulation unit cell in x-direction	21
y	length of simulation unit cell in y-direction	21

II List of Symbols (continued)

Symbol	Meaning	Page
α	Raman polarizability tensor	3
ϵ_r	Relative permittivity	15
$\widetilde{\epsilon}_r$	complex permittivity	15
η	Viscosity of the fluid	16
$\dot{ heta}$	polar angle along a sphere	4
$ heta_1, heta_2$	angle of incidence and angle of refraction	16
λ_i, λ_s	wavelength of excitation field and of the scattered field wavelengths	6
μ_r	Relative permeability	15
ν	Delayed velocity in dispersion relation	15
σ	Conductivity	15
σ_R,σ_S	Raman Scattering cross-section with and without metasurface enhancement	1
ϕ	Azimuth angle along a sphere	4
ψ	The wave function in the Helmholtz equation	4
ω	Angular frequency	4
ω_0	Resonant frequency of resonator	7

1 Introduction

Over the last few years it has become evident that fast and reliable virus detection technologies are essential for dealing with viral outbreaks. Among other things, earlier detection of infection could save patients at risk and prevent transmittance by infected asymptomatic individuals. Currently, the main methods of viral detection rely on assay techniques which involve chemical labeling. Although labeling analysis has become a vital tool in laboratory medicine, the demand for alternate label free methods such as Raman Spectroscopy (RS) increases. This is due to RS's unique advantages: high sensitivity, small working volumes, minimal damage to analytes and possibility of integration with on-chip applications [1]. Label-free methods mainly focus on molecular vibrations which produce fewer false positives than labeling methods and as a result increase the reliability and reproducibility of detection [2]. In addition, RS also is important in chemical analyses, defense and safety, and environmental monitoring applications.

In earlier years, the application of RS was inhibited by its small scattering cross-section of only 1 in 10^{10} photons scattering. This was negligible compared to the Rayleigh scattering and the fluorescence interference predominating the Raman signal. However, since the late eighties hardware advances of detectors, lasers, and filters and improved measurement, and computational techniques RS became viable [3]. Researchers recognized it had the potential to combine "the best of both worlds" with the narrow linewidth and fundamental vibrations found in Fourier Transform Infrared Absorption Spectroscopy with the simple sample handling and water and glass compatibility in Near Infrared Absorption Spectroscopy. In addition, there was the possibility of resonance and surface enhancement. It was not long until RS was applied in a variety of analytical problems [4–8]. One of the techniques applied here used the aforementioned surface enhancement and is appropriately named Surface Enhanced Raman Spectroscopy (SERS). In SERS the average enhancement of a substrate is measured by the relative increase of the Raman scattering cross section σ_R by the SERS cross section σ_S and is called the average SERS Enhancement Factor (EF) [9].

$$EF = \frac{\sigma_S}{\sigma_R} = \frac{I_S N_R}{I_R N_S} \tag{1}$$

EF is often expressed as the Raman scattering intensity without enhancing substrate I_R and with enhancing substrate I_s , and the average number of molecules in the scattering volume without enhancement N_R and average number of molecules present on the substrate in the scattering volume with enhancement N_S .

Despite the fact SERS already has been used for detection of biomolecules, pathogens, and cancer cells [10–13] there are still several issues. The effect of biological interference caused by the SERS substrate, the effect of the biological environment on SERS sensing, and the uncertain origins of changes in SERS spectra are still not fully explored [14]. To advance biological and biomedical applications for SERS, reliable substrates are needed. This requires a high and uniform enhancement, good biocompatibility and the capability to target and trap analytes in hotspots. Currently, popular substrate designs are plasmonic metasurfaces that are randomly roughened. These produce high enhancements, but the random nature of the metasurfaces makes it challenging to reliably manufacture metasurfaces with identical properties such as the large enhancement and uniformity of the Raman shift enhanced Raman signal required in SERS. Further, plasmonics metasurfaces produce a significant amount of heating which could negatively affect biocompatibility. Thus it is important to explore new types of metasurfaces which do not suffer these drawbacks. In the case of SERS, the designs should also meet the previously mentioned properties for bio SERS.

TNO and TU/e recently tried to achieve this by designing a dielectric metasurface exploring Mie resonance for SERS [15]. Dielectrics are known for having substantially lower losses which eliminates the heating problem. They are also very popular in nano-fabrication, especially silicon, and techniques to manufacture many shapes on the substrates are readily available. In addition, during the design of the metasurface, manufacturability and thus reproducibility can be taken into account. However, a major disadvantage of dielectric metasurfaces is the several order lower electromagnetic-enhancement. For this reason they generally perform worse in SERS. It is important to know that surface enhancement in plasmonics is mostly produced by an EM-type enhancement and only a small part through chemical-type enhancements. For dielectrics the chemical enhancement plays a larger role and can even be the main contribution to producing enhancement in SERS. Even so, the chemical enhancement mechanisms are hard to model and are

for this reason not considered during metasurface design.

This metasurface design consisted of an array of pairs of cylinders. Here an unit cell comprises of two silicon cylinders distanced 20 nm apart developed over a gold surface with a fused silical spacer in between. Their design produced an EF of approximately 10^5 in EM-simulations. This was achieved by exploiting two phenomena: the Mie resonance which arises from the coupling between the two cylinders and arises due the geometry of the structure, and the lattice resonances due to periodicity of the dimer on the metasurface. With this knowledge they tuned the parameters of the metasurface such that the narrowband lattice resonance enhanced the electric field of the excitation frequency of the laser and the broadband Mie resonance the Raman shift emission produced by the analytes. The final design produces a strong electric field, or hotspot, in between the gap which gives an high uniform enhancement over all broad range of Raman shift frequencies. Additionally TNO and TU/e investigated trapping and the effects of metasurfaces in immersion. Initially it performed worse due to the lower refractive index contrast. However, after simulating optical trapping they found values similar to the previous metasurface without immersion [16].

Despite the good enhancement, manufacturing of this design is challenging as the large ratio of cylinder height and inter cylinder gap makes the metasurface difficult to manufacture with current nanofabrication techniques. Also, since the highest field enhancement resides within this gap particles larger than 20 nm can not fully be in this spot of high enhancement. Both problems are solved by increasing the gap between the cylinders, but then strength of the Mie resonance between the cylinders significantly decreases which strongly effects the EF. Is there a dielectric metasurface design with a larger gap between the nanostructures that keeps the same EF as the 20 nm gap design in [16]? Could adding more cylinders with different incident light polarization increase EF in this case? Is dry SERS or immersion SERS with optical trapping better for producing high EF?

In this project Electromagnetic (EM) simulation software Lumerical is used to find the field distributions and calculate the EF of the metasurfaces. Different metasurface geometries with larger gaps between structures and excited with both linear and circular polarization will be explored and optimized for best EF. The found field distributions will be used to calculate the EF with optical trapping of different analyte diameters. With the found EFs from the new and reproduced metasurfaces the research questions will be answered.

This thesis is further subdivided in five more chapters. The theory chapter will first discuss theory on a graduate physics level. Here the relevant physics, resonances in SERS, and models for dielectric metasurface design and simulations are discussed. In the methods chapter the methods to setup and test software settings, method of metasurface exploration and optimization, and aspects of computation of optical trapping are discussed. In the results chapter the results of metasurface exploration, comparison between linear and circular polarizations for various metasurfaces, comparison between different optimized metasurfaces, new trapping schemes, and a new metasurface design for better optical trapping are presented and analyzed. In the discussion chapter the results are discussed and recommendations for future work are suggested. In the conclusions section the final conclusions are made and recommendations for future work are proposed.

2 Theory

2.1 Fundamentals

2.1.1 Raman scattering

Photons incident on molecules not only scatter by interacting with the electrons, but can also scatter through interacting with the entire electron cloud. When this happens the electron clouds can become slightly polarized and the molecule enters a virtual state. The photon can scatter elastically named Rayleigh scattering or inelastically through Raman scattering. Raman scattering can occur in two ways: When in an excited vibrational state it can relax to a lower energy vibrational state where the photons gains the energy difference and is named anti-Stokes scattering, and when the molecule is excited to a higher vibrational state the photon loses the energy of difference and is called Stokes scattering. If the photon energy matches the energy difference between the vibrational state and the electronic state than Stokes scattering can also happen by the molecule entering the electronic state and is called resonant Raman scattering. These processes are summarized in fig 1..

The physics of Raman scattering can be better understood from a electrodynamics perspective. By approximating the molecule and its electron cloud as a dipole with dipole moment \boldsymbol{p} which starts to oscillate at frequency v_L under the incident electric field \boldsymbol{E} [17]. \boldsymbol{p} is given by a product of the Raman polarizability tensor α and \boldsymbol{E} . Due to the displacement of the charges by the vibriational modes v_M a perturbation in α dependent on the normal mode coordinate q_k has the following form

$$\alpha(q_k) = \alpha(0) + \left(\frac{\partial \alpha}{\partial q_k}\right)_{q_k = 0} q_k + \frac{1}{2} \left(\frac{\partial^2 \alpha}{\partial q_k^2}\right)_{q_k = 0} q_k^2 + \cdots$$
 (2)

Since α has time varying harmonic components due to vibration, the product αE can be interpreted as the modulation of a signal. The elastic Rayleigh scattered photons with frequency v_L result from the first term in (2), where the molecule and its electron cloud do not deform/vibrate. The next term represents Raman scattering where the molecules and its electron cloud does vibrate over time. In this case the scattered photons have modulated frequencies $v_L + v_M$ for anti-stokes scattering and $v_L - v_M$ for stokes scattering.

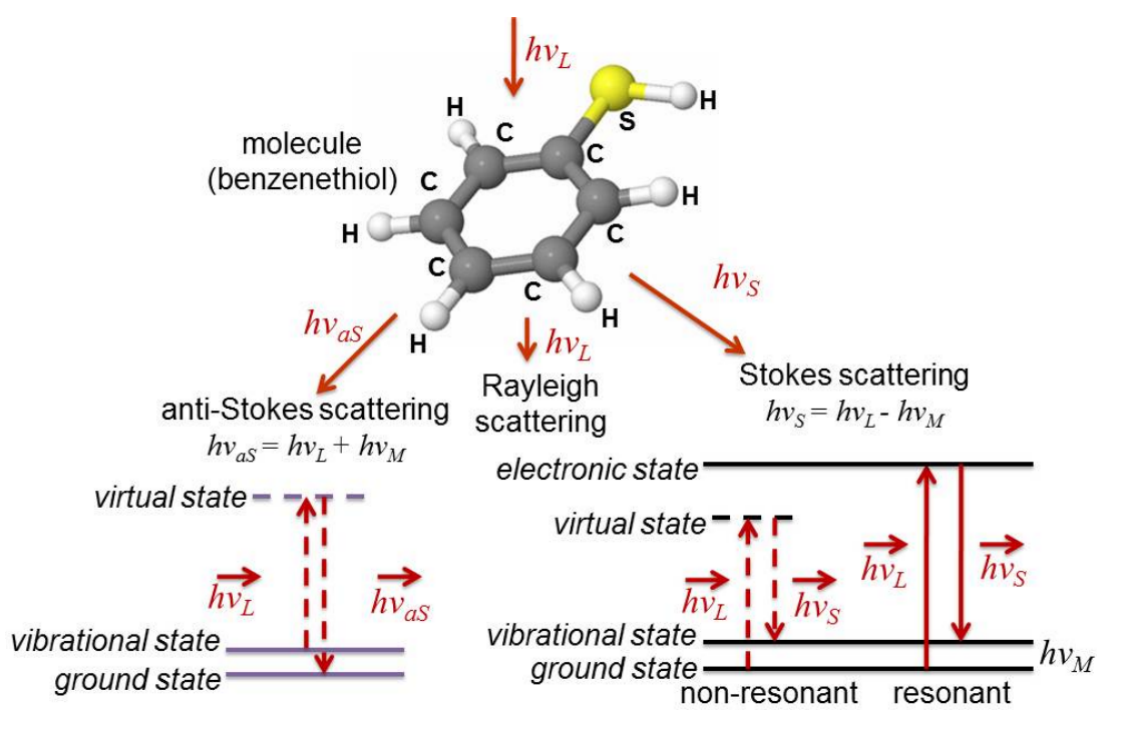


Figure 1: An example of Rayleigh and Raman scattering with benzenethiol [18]

2.1.2 Mie resonances

Understanding how EM fields interact with Nano Particles (NP) is essential to understand the effects of metasurfaces. An exact solution exists for a plane wave scattering by a homogeneous sphere and is often referred as Mie scattering. Mie's solution for homogeneous spheres can be used to gain insight for resonances found for different shaped nano structures. In this solution the incident field is expanded to an infinite combination of vector spherical waves. Essential is the insight that the interface matching conditions can best be satisfied if the EM field is written as a linear combination of transverse electric (TE) and transverse magnetic (TM) spherical waves.

Starting with the ansatz that the vector potential A has the following identity

$$\mathbf{A} = \nabla \times \mathbf{r}u(\mathbf{r}, t) \tag{3}$$

allows to define E and B to be a combination of the spherical TE and TM fields each with u and w as solutions of the scalar Helmholtz equation (4) respectively.

$$[\nabla^2 + k^2] |\psi(\mathbf{r}, t) = 0 \tag{4}$$

Where k is the wave number and ψ a wave function solution. If in addition is assumed that their time dependence is $e^{i\omega t}$ and the dispersion follows $\omega = ck$ then the spherical wave solutions are given in (5)

$$\mathbf{E} = \nabla \times (\mathbf{r}u) - \frac{i}{k} \nabla \times [\nabla \times (\mathbf{r}w)]$$

$$c\mathbf{B} = \nabla \times (\mathbf{r}w) - \frac{i}{k} \nabla \times [\nabla \times (\mathbf{r}u)]$$
(5)

The solution can be found through the method of separation of variables and consists of spherical Bessel radial functions multiplied by spherical harmonic angular functions. The solutions are similar to solutions of the hydrogen atom in quantum mechanics since the Helmholtz equation resembles the Schrodinger equation and the spherical homogeneous sphere the spherical potential the electron is in. The spherical harmonic angular functions are often expressed as a product of sines and cosines for ϕ dependence with the associated Legendre polynomials of the first kind P_l^1 for θ dependence. If a TEM wave in vacuum with an electric field $\mathbf{E_{inc}} = E_0 \exp(ikz)\hat{\mathbf{x}}$ is incident on spherical dielectric then the solution for the incident waves is given in (6)

$$\begin{bmatrix} u_{inc} \\ w_{inc} \end{bmatrix} = E_0 \sum_{l=1}^{\infty} i^l \frac{2l+1}{l(l+1)} j_l(kr) P_l^1(\cos\theta) \begin{bmatrix} \sin\phi \\ \cos\phi \end{bmatrix}$$
 (6)

The solutions for the field inside the sphere and the scattered sphere are similar but inside the sphere k becomes nk. For the scattered field the spherical Hankel function $h_l^{(1)}(kr)$ replaces the spherical Bessel function $j_l(kr)$.

Mie Resonances can arise when an incident wave transiently couples to one of EM normal modes of the dielectric sphere. This can be better understood by analogy with the hydrogen atom by considering these modes as virtual bound states created by the l-dependent effective potential. Here l can be interpreted as the angular momentum of a ray and is given by l = bk where b is the impact parameter. For values of b where it is smaller than the radius R E of the incident ray will refract into the sphere with refractive index n. If b >> R there is negligible interaction between the ray and the sphere. For values of b that are larger than R but not too large the E of the ray can tunnel through the barrier and resonantly excite a normal mode. It will tunnel until the inner turning point b/n and will tunnel back to outer turning point R where it rejoins the ray as illustrated in figure 2. The excited normal modes will evanescently decay out of the sphere giving rise to stronger E and R fields near the surface which is often referred as Mie resonance.

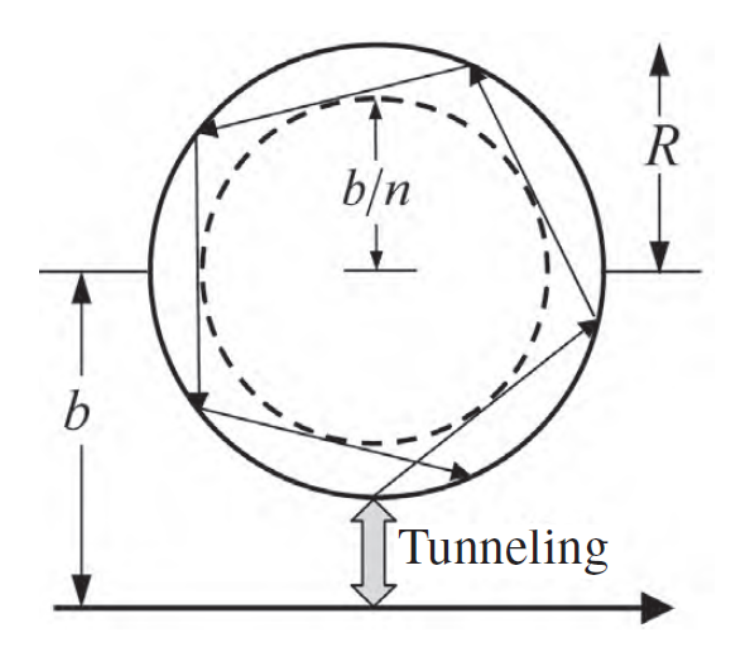


Figure 2: Schematic representation of Mie resonance in homogeneous sphere. The black arrow give the direction of propagation of the light ray and the perpendicular E will tunnel into the NP [19]

2.1.3 Enhancement Factor

There are several challenges in application of EF as expressed in (1). The uncertainty which particles should be counted for N_S , the size of the scattering volume and the non-uniformity of the scattering intensity across the metasurface can create variations up to two order of magnitude. A paper by Le Ru et al [9] gives a thorough analysis for experimental SERS and solutions for these problems. However, for computational analysis of substrate performance their version of EF is difficult to achieve. Factors such as hard to model enhancement mechanisms, variations in detection setups, varying analyte properties all greatly affect EF. Therefore, there are many version of EF for which each relates to a specific type of SERS research.

An EM-enhancement based EF is required in this project as only EM-fields are computed. This can be derived by considering the incident electric field \mathbf{E}_{loc} with frequency v_L on a molecule. This induces a Raman dipole moment $\mathbf{p} = \alpha \mathbf{E}_{loc}$ which emits Raman shifted radiation with frequency v_R with a power proportional to \mathbf{p}^2 . During this process there are two points of enhancement. First, the field exciting the molecule \mathbf{E}_0 can be enhanced by the substrate to \mathbf{E}_{loc} . Here the Raman tensor is isotropic which results in a local field enhancement factor

$$M_{loc} = \left| \mathbf{E}_{Loc} \right|^2 / \left| \mathbf{E}_0 \right|^2 \tag{7}$$

Secondly the Raman dipole emission v_R can be enhanced and the radiation pattern can be altered. For one direction the radiated power is changed by a factor $M_{Rad}(v_R)$. When only interested in back scattering then if it is assumed the Raman dipole aligns perpendicular to the excitation source and the Raman tensor is isotropic, then this term becomes very similar to M_{Loc} . Combining the aforementioned factors results in the following EF of back scattered Raman dipole emission

$$EF = M_{loc}(v_L)M_{Rad}(v_R) = \frac{|\mathbf{E}_{(v_L)}|^2}{|\mathbf{E}_{0}|^2} \frac{|\mathbf{E}_{(v_R)}|^2}{|\mathbf{E}_{0}|^2}$$
(8)

If v_R is approximately the same to v_L then this reduces to the characteristic $|\mathbf{E}|^4$ EF often found in SERS literature. A more elaborate form of this derivation as well as a generalization for EF of unaxial raman tensors can be found in *Rigorous justification of the* $|E|^4$ *enhancement factor in Surface Enhanced Raman Spectroscopy* by Le Ru et al [20].

With this EF from (8) it becomes clear that if the substrate is both resonant at v_L and the Raman shift frequencies v_R very strong enhancements can be created. Metasurfaces can be designed in order to create this combination of resonances. To get an impression of the average EF for

particles randomly placed anywhere on the metasurface averaging integrals are used on (8). The EF for in dry SERS becomes

$$EF(\lambda_e) = \frac{1}{A} \int_S \left| \frac{E(\lambda_i, \mathbf{r})}{E_0} \right|^2 \left| \frac{E(\lambda_s, \mathbf{r})}{E_0} \right|^2 dS$$
 (9)

and for particles somewhere randomly in the volume for immersion SERS

$$EF(\lambda_e) = \frac{1}{V} \int_V \left| \frac{E(\lambda_i, \mathbf{r})}{E_0} \right|^2 \left| \frac{E(\lambda_s, \mathbf{r})}{E_0} \right|^2 dV$$
 (10)

Where S is the surface of unit cell metasurface, V is the scattering volume in the unit cell, λ_i is the wavelength of excitation field, λ_s is the wavelength of the scattered wavelengths.

When selecting the incident laser wavelength the following needs to be considered. Just as in Rayleigh scattering the cross-section of RS is proportional to the inverse fourth power of the excitation wavelength meaning that halving the wavelength results in 16 times higher RS intensity. But for VIS and UV wavelengths most organic and biological molecules undergo auto-fluorescence which obscures the Raman signal. This is a large contributor for the industries choice to selected the NIR wavelength of 785 nm as one of the standards. Solutions are developed to address this such as preparatory photo-bleaching [21] and better post-measurement processing through polynomial fitting [22]. The choice for the frequency range of the Raman shift region highly depends on the target analyte. Generally Raman shift range between 200 cm⁻¹ and 1400 cm⁻¹ suffices for capturing the distinct sections of the Raman spectrum of the analytes.

2.2 **SERS**

2.2.1 Plasmonics

Shortly after the discovery of single molecule SERS a theoretical framework for metal-assisted SERS was formulated and the field of was plasmonics founded [23]. This theory treats the core phenomenon, propagating electron oscillations named surface plasmons (SPs), mainly from an electrodynamic view. Here SPs are regarded as a surface wave. These surface waves are defined as guided waves propagating parallel to the surface. Here they satisfy the Sommerfeld radiation condition which means that in both orthogonal directions as the waves approach infinity they must either propagate away from the surface or vanish; the SP is the only source. This leads to solutions of the surface waves which can be seen as homogeneous solutions of the Maxwell equations. When the SPs couple to the longitudinal charge density wave in the material then Plasmon Polaritons arise. Surface Plasmon Polaritons (SPPs) are longitudinal waves propagating along the interface between a dielectric and a metal. To generate SPPs momentum matching techniques are needed to overcome the momentum mismatch. This can be done by illuminating under an angle from a high refractive index dielectric medium or by using a grating on top of the interface. Another popular technique imposes physical boundaries through metallic nanoparticles or sharp edges. Here SPs are bound to the structure and do not propagate like the SPPs and are therefor called Localized Surface Plasmons (LSPs). The optical properties of LSPs are mostly determined by the geometry and changing this allows to tune the Raman spectra and localize and enhance fields near the particles [24].

2.2.2 Localized Surface Plasmon resonances

Plasmonics also finds a lot of interest in the fields of optical signal processing, nanoscale optical devices, and near-field microscopy [25]. Many materials and geometries of NPs and metasurfaces have been investigated. The most popular metals used are gold, silver, copper, and aluminium [26]. Substantial research is devoted in exploring different plasmonic materials for applications in different spectral ranges with different plasmonic effects [26–28]. One of the most popular geometries in research is the sphere. This is not a coincide as the longstanding theory of Gustav Mie offers an analytical solution to the LSPs on the surface of a sphere allowing to compare theory to numerical and experimental results [29]. This analytical solution is still being extended to a broader set of cases such as metal NP resonances with different shapes [30, 31]. Modifying the shapes of the NPs lead to different optical properties. Elongating NPs give an anisotropic response and can be used to localize hotspots and tune the properties through aspect ratio. Popular applications are

nanorods [32, 33] and ellipsoids [34]. Another way to vary is by applying asymmetric NPs which enables Fano-like sharp line shapes and possibility to manipulate the polarization of the incident light. L- and U-shapes [35] and spiral shapes [36] have been shown to have such behavior. One of the most important geometric properties for SERS metal NPs is the relation between the curvature and the field enhancement. High curvature, sharpness or roughness metallic NPs result in very high localized fields in plasmonic materials [24, 37]. The optical properties for high curvature morphologies such as nanostars [38, 39], nanoflowers [40, 41], nanotips [42, 43], nanocrescents [44] as well as different types of rough planes [45] have been investigated. Recent developments introduced roughened NPs such as roughened nanospheres and nanorods showing abundant spots of field enhancements [46, 47].

The energy storing capabilities of NPs is often expressed through the quality factor (Q) and is given as

$$Q = \omega_0 \frac{S_E}{L_E} = \frac{\omega_0}{\delta \omega} \tag{11}$$

Here ω_0 is the resonance frequency, S_E the energy stored per cycle, L_E the energy losses per cycle, and $\delta\omega$ the FWHM of the resonant frequency. High Q NPs function as optical resonators that can propagate evanescent waves tangent to the NP surface for several hundreds of nanometers. It should be noted that metasurface configurations with single NPs has a limited Q, thus also limited local field enhancements. The quasi-static approximation of Weng & Sheng shows that to the first order the quality factor Q only depends on the dielectric function of the NP and is thus independent of shape or refractive index contrast between interfaces [48]. A way to get around this is by placing other NPs close to the single NP as shown in fig (3) or putting them in a periodic array. Subsequently, the two NPs (dimer) gap distance and unitcell size become new degrees of freedom for tuning the metasurface to desired optical properties. By doing this the LSPs of each NP can electromagnetically couple and enable strong localized electric field resonances between the closest point of contact, called hotspots, as seen for the spherical gold NP dimer in fig (4). In addition, the array of NPs can be seen as a grating which will produce diffraction orders which can lead to strong resonances and field enhancements between the NPs [49–51]. The latter will be discussed more in depth in a later section. The types of Localized Surface Plasmon Resonances (LSPR) possible depends heavily on the geometry of NPs. For example, elongating a nanosphere into a ellipsoid allows for the degenerate longitudinal and transverse modes dipole modes, due to spherical symmetry, to be split resulting into two separate resonant modes due to anisotropy [52]. In rice shaped NPs elongation created multipolar modes [53] and employing multipolar resonances results in better polarizability and as a result a better E enhancement. A simplistic representation of this effect of geometry is given in fig (5).

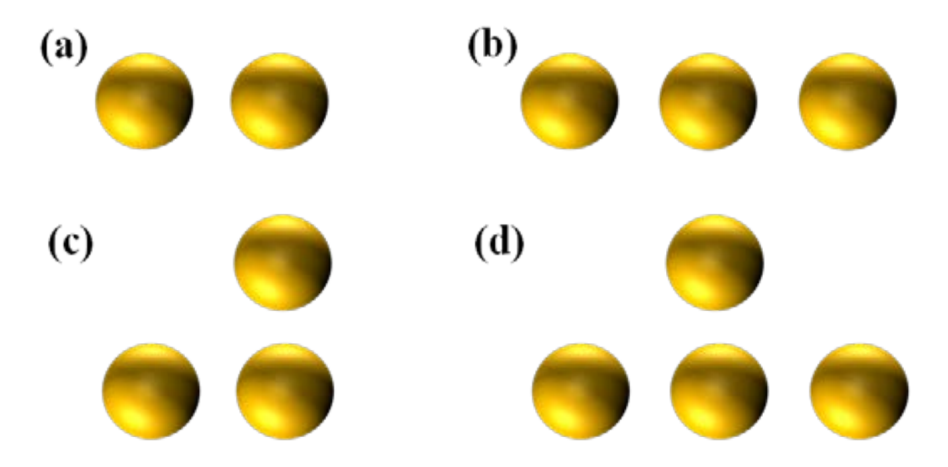


Figure 3: a-d different unitcell configurations of spherical gold particles [52].

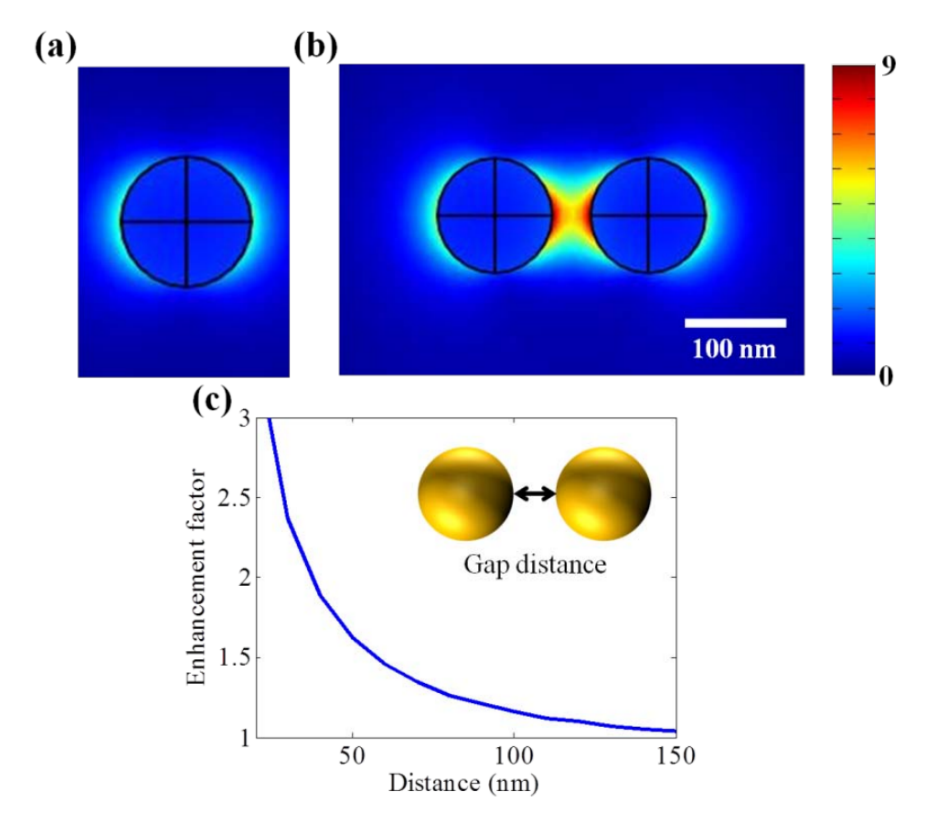


Figure 4: Simulation of the normalized electric field enhancements for single and dimer 50nm radius Au nanoparticles: (a) Field single Au np. (b) Field dimer Au NP. (c) The enhancement factor against dimer gap size for Au dimer [52].

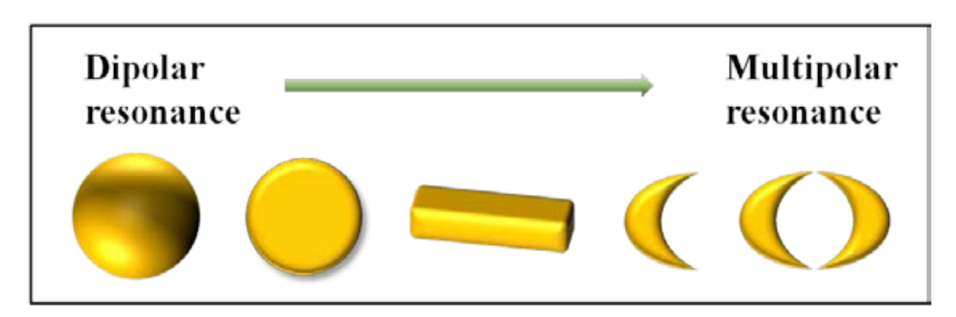


Figure 5: Diagram showing spherical and smooth NPs have strong dipolar LSPRs (left) while elongated and sharp NPs have strong multipolar LSPRs (right) [52].

In configurations such as dimers the illumination polarization becomes an important factor for tuning optical properties and field localization. If the electric field of a normal incident plane wave is polarized along the dimer axis, the line passing through the centre of each NP, then stronger electric fields are localized in between them like in fig 6ac. However when the incident E-field is orthogonal to the dimer-axis the enhancement is weakened and localized outside the gap see fig 6b-d [54]. Albella et al. [55] applied a dipole approximation and numerical Finite Difference Time Domain (FDTD) simulations for the orthogonal incident E-field in dielectric dimers and found they also can create strong magnetic field enhancement. Additionally they identified two regimes: a strong coupling regime were the dimer gap is small and the dipole approximation does not give a good approximation compared with the FDTD results, and a weak-coupling regime were the dipole component is predominant and gives a good approximation to the expected field strength. Another way the enhancement can be affected is by changing from normal incidence to oblique incidence. Changing to oblique incidence often reduces enhancement by LSPs although it can give access to higher order resonances in periodic structures [49, 56].

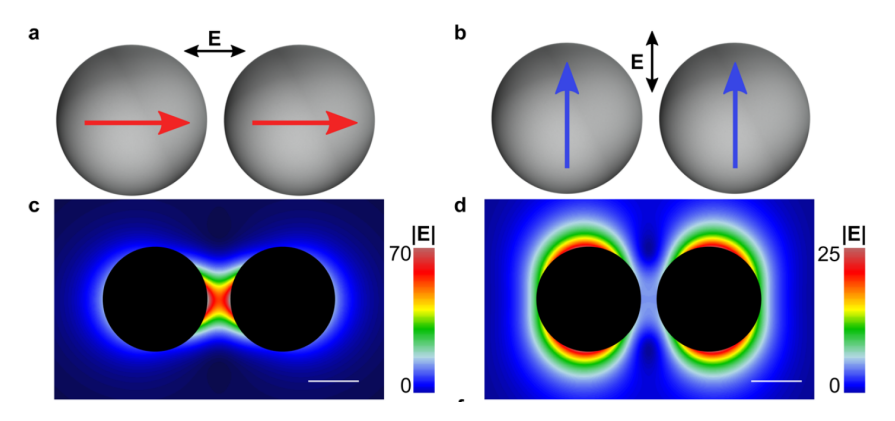


Figure 6: **a-b** Direction of LSPRs for x-polarized (**a**) or y polarized electric fields (**b**. **c-d** Intensity of LSPRs for x-polarized (**c**) or y polarized electric fields (**d** [54]

2.2.3 Dielectric SERS

Non-metal or high and positive refractive index dielectric materials are also popular as they are known for their low losses and have already been used a lot in manufacturing nanostructures [57, 58]. In dielectric NPs the resonances results from the displacement currents instead of the longitudinally moving electrons in SPs which cause friction and thus losses and joule heating. Another large advantage of dielectrics is the high presence of both electric and magnetic resonances which in plasmonics are hard to sustain at the same time [59]. Coupling between the electric- and magnetic modes allows for new optical properties. An example of this is the Kerker effect where the electric- and magnetic dipole modes couple and backwards scattering is completely suppressed [60]. Most of the theoretical frameworks designed for plasmonics can also be applied to dielectrics since only the dielectric constant changes. A major drawback of switching to dielectric materials is the lower field enhancement associated with dielectric substrates compared to plasmonic ones. Despite the low enhancements, the field of dielectric SERS grew and according to Alessandri et al. the number of papers went up from a few to 30 each year between 2005 and 2015 [61].

Randomly roughened or colloidal metasurfaces are not as effective in dielectrics SERS for creating hotspots and mostly relies on chemical mechanisms such as Charge Transfer (CT). In periodic array NP structures however, EM-enhancement can generate a high density of hotspots [15]. Given that the wavelengths are approximately the size of the NPs, then to understand the fields generated in such a metasurface Mie theory can be used to to offer insights into fields of other NP geometries. The Mie regimes for spherical NPs can be made more concrete using the size parameter s given by (12) below.

$$s = \frac{2\pi R}{\lambda} \tag{12}$$

The Mie regime is in the range of 0.1 < s < 100. Within the Mie regime possible modes correspond to the electric and magnetic dipole, quadrupole and higher modes. The TE, in this case expressed by $TE_{i,j}$, TM, labeled $TM_{i,j}$, modes where the first index i is number of maxima in the half sphere period and the second index j is number of maxima in the radial direction. The $TE_{1,1}$ and $TM_{1,1}$ modes belong to magnetic dipole (MD) and electric dipole (ED) modes respectively and a have distribution on the sphere as seen in fig 7. Just as in plasmonics, the harmonics found depend on the shape of the potential barrier. Dielectric microspheres in the range of 30 to 300 micrometer have high Q in the range of $10^7 - 10^9$ and have been shown to be effective for biosensing [62]. Still, small shape distortions, surface inhomogeneities and absorption can strongly reduce Q [63]. Lastly, high values for Q do not necessarily mean a high EF from the substrate.

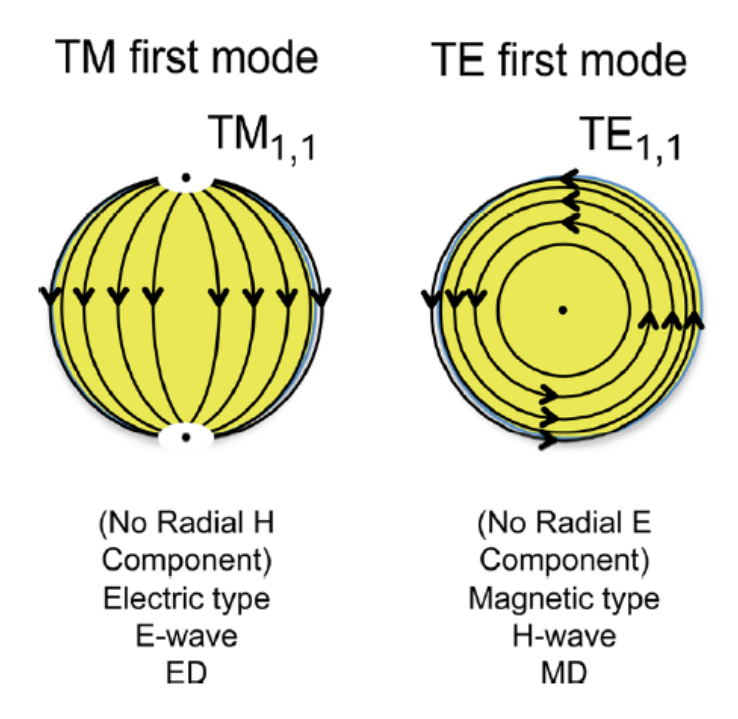


Figure 7: Schematic representation of the displacement fields in dielectric nanospheres. Left the first electric dipole mode and right the first magnetic dipole mode [61]

2.2.4 Surface lattice resonances

Surface Lattice Resonances (SLR) are another type of resonance that can be exploited in combination with the Mie Resonances. These resonances are known to have high Q and are capable of coupling NPs over large distances. SLRs are enabled by the diffracted orders when a plane wave hits a periodic structure. When a plane wave hits a periodic structure with periodicity D_x in the x-direction then the passing plane wave gets the same periodicity D_x in this direction. The periodic structure "chops" the wave front and since the field must be continuous only certain allowed directions can be sustained [64]. The power is send in multiple discrete directions named diffraction orders. For periodicity in the x direction this results in different waves with wavenumbers that are dependent on the order m and D_x as in (13)

$$k_x = k_{x,inc} \pm \frac{2\pi m}{D_x} \tag{13}$$

For phase matching with periodic structures or gratings, only the tangential components are considered and solutions for the directions of the diffracted orders of (13) can be found for the reflected and transmitted waves. Different array configurations can be explored for desired resonance properties. The most common is a 2D square array with period D, incident medium refractive index n_2 , substrate refractive index n_1 , angle of incidence θ and m and p the diffracted order numbers this becomes (14)

$$\lambda_{m,p} = D \frac{\sqrt{n_2^2(m^2 + p^2) - n_1^2 p^2 \sin^2 \theta} \pm m n_1 \sin \theta}{m^2 + p^2}$$
 (14)

At normal incidence the first diffracted order, (0,1) and (1,0), from (14) is degenerate and the period simplifies to the wavelength in the incident medium. This theory however is incapable of predicting the wavelength and magnitude of the SLR wavelength.

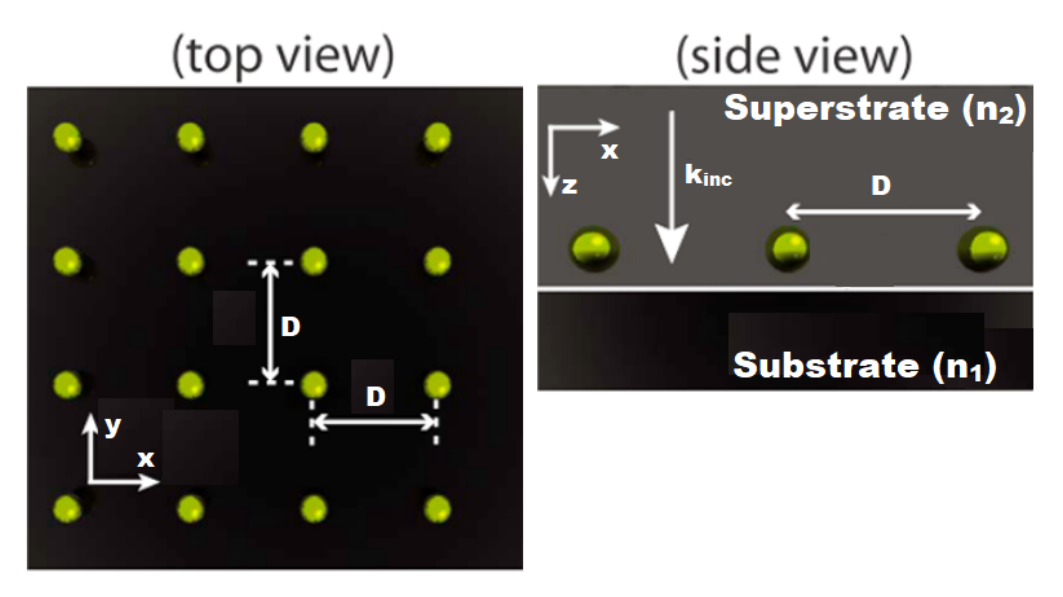


Figure 8: Schematic representation of the top view and the side view of a square lattice of period D of gold nanospheres. [49]

.

The coupled dipole approximation (CDA) offers a solution to this by approximating NPs in periodic structures as a lattice of small polarizable electric dipoles [65, 66]. CDA has been used for the prediction of diffraction coupled resonances [67–70]. Assuming an infinite array of identical particles with the same polarizability α_S , which can be calculated through EM-theory, an expression can be found for the polarization P is

$$P = \frac{E_0}{1/\alpha_s - S_{dip}} \tag{15}$$

where E_0 is the electric field amplitude of the incident wave and S_{dip} is the retarded dipole sum. With P obtained from (15), the extinction cross-section C_{ext} of one particle can then be expressed as (16).

$$C_{ext} = 4\pi k \operatorname{Im}\{P/E_0\} \tag{16}$$

In this case C_{ext} entirely depends on the complex part of P. When the real parts of $1/\alpha_S$ and S_{dip} approach each other then the real part of P becomes very large and high resonances become possible. This condition for SLRs is the same as for LSPRs. Humphrey and Barnes investigated the extinction cross-section with the extended CDA approximation, which incorporates the finite NP size, for a square array of silver disks the results are given in the graphs of fig 9 [71]. From (14) the calculated SLR wavelength is 727 nm which is blue-shifted compared to the measured 760 nm. CDA gives a SLR wavelength if 780 nm and is slightly red-shifted compared to the measurement. There are two points wavelengths were SLRs are possible indicated in the middle and right graph of fig 9 by black vertical dotted lines. By looking at the complex parts of S_{dip} and $1/\alpha_S$ it can be seen that the low wavelength resonance is damped, because the complex part of the denominator is large in (15). For the second resonance the denominator is smaller and thus lead to a larger extinction cross-section allowing the resonance.

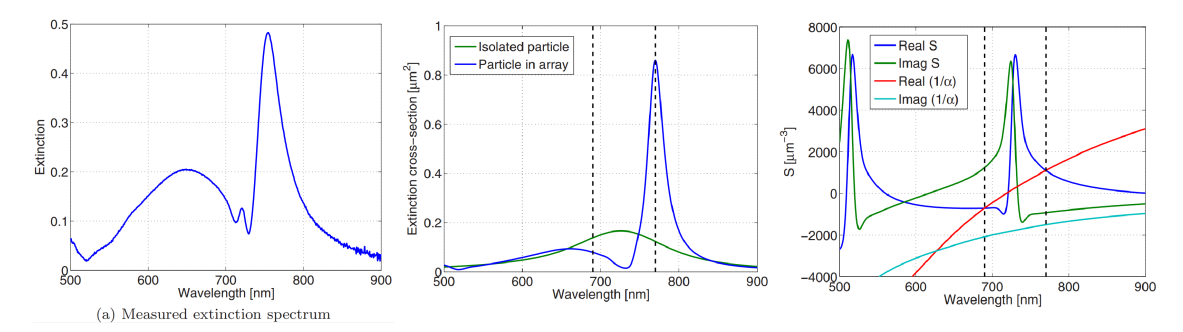


Figure 9: Extinction spectra and dipole sum as function of wavelength for a square lattice of period 480 nm of silver disks with height 30 nm and diameter 120 nm. Light is linearly polarized along the arrays y-axis and is normally incident. The substrate was in immersion oil of n=1.515 and using (14) gives (1,0)/(0,1) diffraction order at 727 nm. Left: the measured extinction for structure. Middle: calculated extinction cross-section per particle. Right: Real and complex parts of the S and $1/\alpha_S$ components of the polarization in (15) [71]

.

Multiple factors can affect SLR generation on substrates. Most importantly there is the lattice period which can be used to tune the SLRs, as to couple the SLRs with the LSPRs or Mie resonances which can create very narrow and high resonances. Two regions can be defined: the region were the wavelength of the diffraction edge is lower than the LSPR wavelength, in this case very little coupling occurs, and the other region where the diffraction edge is larger than LSPR wavelength. In this case for increasing period the SLR becomes higher and narrow up till a certain wavelength from which it will decrease in intensity as seen in fig 10 [72]. Research was also done on the effect of disorder in the array [73]. For gold nanocylinders it was observed that for increasing positional disorder the SLRs slightly blue-shifted and weakened, and for increasing disorder in particle size a broadening of the resonance is observed [74]. As the sizes of particles differ, the LSPRs are different and only a smaller part of NPs will coherently couple for a specific wavelength. Lastly a way to vary the resonance is through different lattice geometries and looked at the resonances of square, rectangular, hexagonal, and honeycomb lattices [71]. They varied the period in the x-direction D_x of silver disk rectangular lattices and learned that under x-polarized light SLR wavelengths and intensities stay roughly the same. However, under y-polarized light the SLR was broadened and blue-shifted given $D_x < D_y$. For $D_x > D_y$ the SLR was narrower and red-shifted. For the hexagonal and honeycomb structures the SLRs had roughly the same wavelengths.

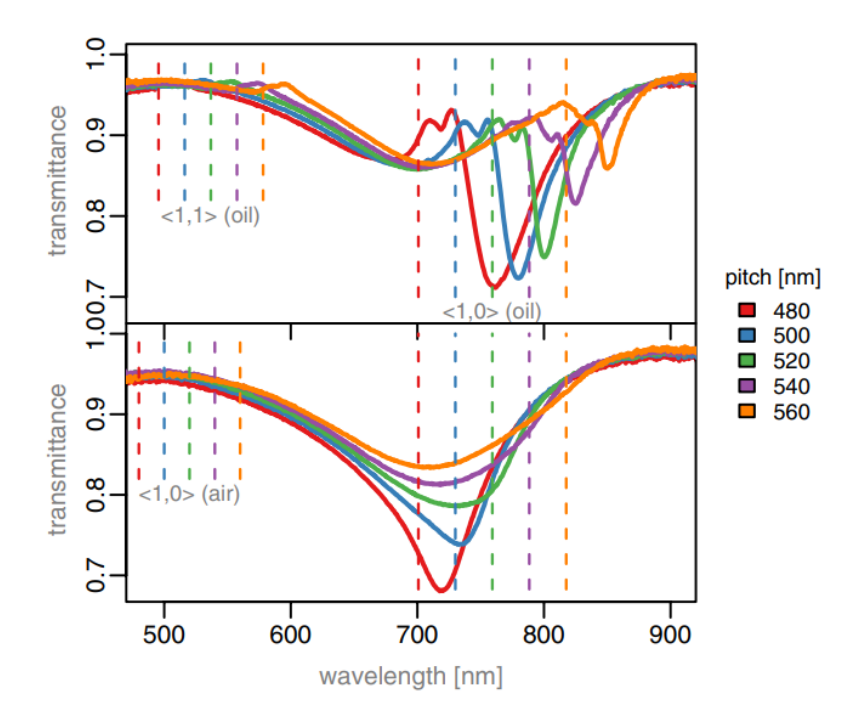


Figure 10: Transmittance spectra of the SLR resonances of Au nanorod arrays in different environment mediums for different lattice periods. **Top** immersion oil (n=1.46) is used and has a small (1,1) resonance in the optical region and (1,0) resonance in NIR region. **Bottom** air in the optical region the (1,0) resonance and NIR region the diagonal grating (1,0) resonance. [72]

Besides lattice structure, factors such as refractive index of the medium, illumination conditions and NP geometry play a role in generation of SLRs. Reflections caused by refractive index contrast between the superstrate and the substrate have been observed to inhibit SLRs [72, 74]. However, for large NPs the contribution of these reflections compared to the total array reflection becomes small. A refractive index matched superstrate-substrate index matching is only necessary if the NPs are small, around 35 nm at NIR frequencies, and normal incidence is needed [72, 75].

2.3 EFs of hotspots found in metasurfaces

2.3.1 SERS hotspots

Together with LSPs or Mie Resonances, SLRs can be used in plasmonic and dielectric SERS to create hotspots. Le Ru et al [76] provided a useful theoretical framework to understand SERS. Here they demonstrate that for large EFs only the particles in the hotspots give a non-negligible contribution to the overall SERS signal and that the probability density function of the EF follows a power law distribution in this case. Additionally, to get an impression about EFs, they note that for Single Molecule-SERS (SM-SERS) enhancement factors of $10^8 - 10^{10}$ are needed which, as previously mentioned, was already shown to be possible for plasmonic SERS. For SM-SERS concentrations it is improbable the target molecule ends up in one of the hotspots. One can redesign the metasurface such that a larger volume of hotspots increases the likelihood of particles falling into this region. Langmuir-Blogdgett assemblies have been reported to be a powerful technique to achieve this [77, 78]. Alternatively, wrinkled and warped substrates have also been show to increase the hotspot density [79, 80]. Instead of relying on random absorption several methods can be employed to direct the molecules towards the hotspots. Lin et al. [81] found positive ion mobilization into the hotspots centimeters away by applying a bias voltage and also designed an array of "nanolenses" surrounded by positive charges to gain more control for particle localization. Another technique uses a bias voltage to trap low concentration particles in immersion within a nanoslit/nanopore and even managed to trap the particle for several minutes by carefully balancing the electroosmotic, electrophoretic and plasmonic gradient forces [82, 83].

2.3.2 Enhancement fields by dielectric metasurfaces

One paper by Černigoj et al. [15] reported the possibility to exploit the prior requirement through tuning the geometry of an array of cylindrical silicon dimers on a gold surface such that the (1,0)/(0,1) narrowband SLR resonance was resonant at the excitation wavelength and the broadband geometry dependent Mie resonance was resonant at the relevant Raman shift wavelengths. Average EFs of around 10^5 through numerical FEM were reported. Cambiasso et al. [84] found for an array of cylindrical silicon dimers on Al_2O_3 substrate with 22 nm gap from experiment a max EF of around 2000. X. Ao [85] looked into a lattice of silicon ellipsoid dimers on gold where the long axis is orthogonal to the gap direction. From numerical methods, a gap of 50 nm gave a max EF of 3000 and a gap of 150 nm gave a max EF of 900.

Some different dielectrics such as a thin film of rough ZnSe can yield an maximum EF of 10⁶ enabled by both EM and CT mechanisms [86, 87]. Livingstone et al. [88] experimented with CdSe quantum dots and found strong maximum EF of 10⁵ mediated by the CT mechanism. Lastly several metal oxides have been also been proven to have potential as dielectric metasurfaces. A rough surface made out TiO₂ nanofibers were found to have high maximum EFs around 10⁶ which were produced by multiple mechanisms [89]. Several different shapes of FE₂O₃ NPs placed on a quartz surface gave maximum EFs of 10⁴ enabled through CT [90]. Another study found for 20 nm ZnO nanocrystals maximum EFs of 10³ also through CT [91].

2.3.3 Enhancement fields through hybrids and holes

The most popular solution for the high losses of plasmonics was to turn to metal-dielectric hybrid materials. Combining both the low losses of dielectrics and high enhancements of noble-metals. Common are the dielectric-metal core shell configurations for example spherical Si-Au core-shell spheres with maximum EFs of 10⁸ utilizing mainly EM enhancement [92]. Another configuration is the dielectric Nanorod with smaller metal particles such as the ZnO nanorod array with Ag NP of Huang et al.[93] with maximum EFs of 10⁹. For Te nanowires with tunable Au NPs the same maximum EFs were found [94]. The EFs of hybrid structures can potentially even be further enhanced by increasing the CT mechanism through transitional metal ion doping, giving especially better resonances in the optical regime [95, 96]. One aspect in hybrids to be careful of is the potentially reduced photostability of the analytes bound to the structure [97].

A totally different approach to metasurfaces is through nanoholes (NHs) instead of NPs. For flow-over noble-metal nanohole arrays maximum EFs of between $10^5 - 10^7$ were found [98, 99]. An advantage of this setup was that the nanoholes larger dimensions compared to a NP for observing the same spectral wavelength makes them easier to manufacture. [98]. In addition they can easily be used to couple SPPs, LSPRs, and SLRs and create strong and uniformly distributed hotspots [99]. Lastly an unique feature of NHs is the possibility of flow-through sensing which is a very promising configuration for on chip sensing in immersion. Although proving some new design challenges, C. Escobedo [100] summarizes the following potential benefits: enhanced transport to in-hole active areas, rapid in-hole cross-stream diffusion of analytes, flow parallelization and solution sieving, high efficiency utilization of analyte, and fast response during sensing.

2.4 Finite Difference Time Domain method

Exact solutions like presented in Mie Theory are not available for most geometries, and therefor numerical solutions of the Maxwell's equation are needed. A popular method is FDTD first developed by K. S. Yee and presented in 1966 [101]. FDTD is popular as it is capable of assessing a wide frequency range in a single simulation and can also easily be applied to calculate quantities such as the Poynting vector and transmission and reflection spectra with Fourier transforms [102].

The FDTD method belongs the class of the grid-based numerical finite difference methods. In this case central-difference approximations are applied on both the space and time partial derivatives of the differential form of the Maxwell equations. Subsequently, the E and H field vector components are solved at every n and $n + \frac{1}{2}$ time step respectively in a "leapfrog" manner. Instead of using a collocated grid it is common practice to use a Yee grid. Here the fields components are staggered within the grid cell as seen in fig 11 and is called a Yee cell. This type of grid cell is most compatible with a Cartesian grid. The motivations stem from the resulting divergence free fields, easy implementation for the matching conditions and its ability to approximate the curl equations [64]. The consequence of having field components at a physically different positions is

that they are out of phase and some may be in different media. To resolve the latter these are assigned their own material properties. The prior influences the dispersion in the Yee grid from the classic dispersion for an isotropic materials as in (17)

$$\left(\frac{\omega}{c}\right)\mu_r\epsilon_r = k_x^2 + k_y^2 + k_z^2 \tag{17}$$

to the dispersion relation on a frequency-domain Yee grid (18) which has an highly anisotropic dispersion.

$$\left(\frac{\omega}{\nu}\right)\mu_r\epsilon_r = \left[\frac{2}{\Delta_x}\sin\left(\frac{k_x\Delta_x}{2}\right)\right]^2 + \left[\frac{2}{\Delta_y}\sin\left(\frac{k_y\Delta_y}{2}\right)\right]^2 + \left[\frac{2}{\Delta_z}\sin\left(\frac{k_z\Delta_z}{2}\right)\right]^2 \tag{18}$$

Here Δ_i is the width of a grid cell in direction *i*. To reduce this numerical dispersion and thus the delayed velocity ν a compensation factor can be used to change the ϵ_r and μ_r that artificially speeds up the wave. It must be noted this method only completely removes this numerical dispersion in a single direction of k and only mitigates for one choice of ϵ_r and μ_r .

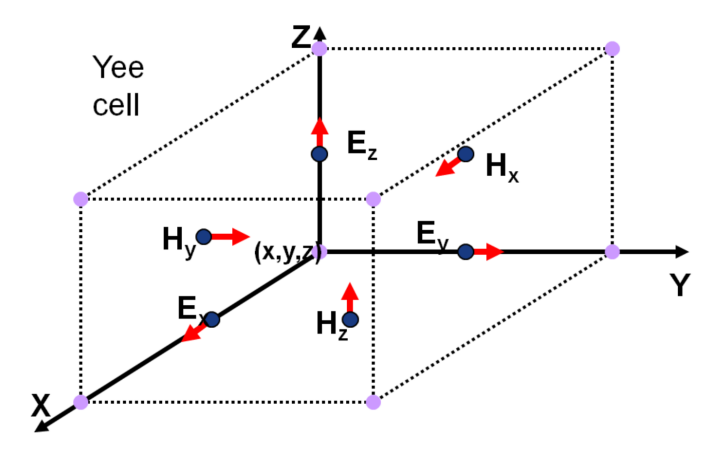


Figure 11: Schematic representation of the Yee cell [102]

The boundaries in FDTD are either the absorbing type, or the periodic type. Physically, absorbing boundaries are supposed to simulate an infinitely extending space which is characterized by total transmittance of EM radiation. Completely absorbing boundaries have a similar effect on the the simulation region. Perfectly Matched Layers (PML) are a popular type of absorbing boundaries in FDTD designed to minimize reflections. For isotropic materials it follows from the Fresnel equations that reflections can be eliminated for only one frequency, angle and polarization. Unaxial PMLs solve this by using doubly-diagonally anisotropic boundary materials. First the complex permittivity $\tilde{\epsilon}_r$ as in (19) needs to be defined.

$$\tilde{\epsilon}_r = \epsilon_r + \frac{\sigma}{j\omega\epsilon_0} \tag{19}$$

Where σ is the conductivity. This expression can be found by changing the Maxwell magnetic field curl equation to its frequency domain form and applying the free current $j_f = \sigma E$. A similar way the same form can be found for the complex permeability $\tilde{\mu}_r$. $\tilde{\epsilon}_r$ and $\tilde{\mu}_r$ are now both diagonal tensors and can be defined for each boundary, then to reduce reflections they are impedance matched by equating the tensors. This results in a form of the tensors as given in (20) where a, b and c are the xx-yy-zz direction elements of $\tilde{\mu}_r$ and $\tilde{\epsilon}_r$ respectively.

$$[\epsilon_r] = [\mu_r] = \begin{bmatrix} a & 0 & 0 \\ 0 & b & 0 \\ 0 & 0 & c \end{bmatrix}$$
 (20)

Then for a double-anisotropic interface Snells law can be reduced to (21)

$$\sin \theta_1 = \sqrt{bc} \sin \theta_2 \tag{21}$$

and Fresnel equations of reflection for TE and TM polarizations to (22).

$$r_{TE} = \frac{\sqrt{a}\cos\theta_1 - \sqrt{b}\cos\theta_2}{\sqrt{a}\cos\theta_1 + \sqrt{b}\cos\theta_2}$$

$$r_{TM} = \frac{-\sqrt{a}\cos\theta_1 + \sqrt{b}\cos\theta_2}{\sqrt{a}\cos\theta_1 + \sqrt{b}\cos\theta_2}$$
(22)

Finally it can be shown that for b=1/c then there is no refraction since the angle of incidence θ_1 must be equal to the angle of refraction θ_2 or $\theta_1=\theta_2$. Combine this result with a=b then r_{TE} and T_{TM} becomes 0. This will be the case for any frequency, polarization and angle. The resulting unaxial tensors can be formulated this way for every boundary. They are then multiplied to arrive at the final PML tensor [S] (23).

$$[S] = \begin{bmatrix} S_x^{-1} S_y S_z & 0 & 0\\ 0 & S_x S_y^{-1} S_Z & 0\\ 0 & 0 & S_x S_y S_z^{-1} \end{bmatrix}$$
(23)

The final Maxwell equations then contain [S] after the material tensors.

Another PML boundary method named convolutional PML relies on taking the inverse $[S]^{-1}$ on both of the Maxwell equations which effectively "stretches" the coordinates. Convolutional PML is less computationally expensive and is currently the state of art, however it does not have a clear physical interpretation as unaxial PMLs. Generally PMLs perform optimally when σ is gradually increased over its multiple layers. To simulate periodic structures periodic boundaries can be used. In the case of incident light at angles a bloch type boundary can be used. Bloch type boundaries are computationally expensive so should be avoided if not needed. Lastly it is possible to exploit symmetry in periodic structures with symmetric and anti-symmetric boundary conditions.

2.5 Optical trapping

2.5.1 Dielectrophoresis

Uncharged dielectric particles exposed to a non-uniform electric field are subject to a force in a process called dielectrophoresis. Here the electric field gradient polarizes the particle inducing a dipole. As the field is non-uniform, one of its poles experiences a larger electric force than the other resulting in a net force [103]. An expression for the dielectrophoretic force F_e exists for a homogeneous sphere with radius r_p and complex permittivity ϵ_p floating in a dielectric medium with complex permittivity ϵ_f subject to the gradient of the electric field ∇E and has the form

$$F_e = 2\pi r_p^3 \epsilon_0 Re(\epsilon_f) Re\left(\frac{\epsilon_o - \epsilon_f}{\epsilon_p + 2\epsilon_f}\right) \nabla |E|^2$$
(24)

Effective optical trapping becomes possible when F_e is greater than the root mean squared Brownian force $F_B(t)_{RMS}$. The Langevin description can be used to calculate the Root mean squared Brownian force. If it is assumed F_B has zero mean and is independent of particle velocity than the Brownian force can be well approximated by a zero mean stationary Gaussian process [104]. Its auto-correlation function is then

$$\langle F_B(t)F_B(t')\rangle = 2\mathcal{D}\delta(t - t') \tag{25}$$

where the constant $\mathcal{D} = 6\pi r_p \eta k_B T$ where k_b is the Boltzman constant, η is viscosity of the fluid, and T is the temperature. By taking the root of (25) at t = t' than the root mean square browning force can be defined as

$$F_{B,RMS} = \sqrt{\langle F_B(t)F_B(t')\rangle} = \sqrt{2D}$$
 (26)

The $F_{B,RMS}$ only has one particle dependent parameter which is the radius. Equating the two forces (24) and (26) yields a results where the gradient field depends on the particle radius through the following relationship $\nabla |E|^2 \propto 1/r_p^{\frac{5}{2}}$. This means that trapping smaller particles is harder and requires stronger electric field gradients.

2.5.2 Optical trapping in SERS

Normally in a dry SERS setup, a droplet with a certain concentration of analyte is placed on the metasurface. After some time, the water has evaporated and the analyte particles are randomly positioned on the metasurface and RS is executed. This evaporation is important for plasmonic SERS as strong hotspots are found very near to the sharp features of the substrate. But for low concentrations, as in SM-SERS, this method can pose a problem, as the particle might not end up in these hotspots. Optical trapping by exciting the metasurface in immersion can allow particles with a refractive index larger than the surrounding medium to be attracted by the electric field gradient forces of these hotspots, if these are large enough compared to the forces caused by random thermal fluctuations [105]. Lastly laser power and exposure time affect the quality of trapping. Longer exposure times and higher laser intensity generally result in better trapping, but for high laser intensities there is the risk than analyte particles become trapped in local maxima or lower intensity hotspots. [16, 106].

In a random roughened plasmonic or dielectric metasurfaces it is best to continue optical trapping until the analyte solution is completely evaporated as the dielectric constant of air gives a higher magnitude polarizability than water, thus a better electric field enhancement [24]. But for metasurfaces where the hotspots reside between large NPs, and thus not on some patches on the surface of the substrate, this becomes less obvious as the optical trapping plus immersion could allow several analyte particles to float in the hotspot and give a larger EF than just for dry SERS were some particles "stick" to the NPs. Especially when the gap between such structures becomes larger this would increase the advantage of immersion SERS.

Optical trapping with plasmonic SERS has already been demostrated several times [107–111]. Strobia et al. [112] tried to improve the overall sensitivity and reproducibility of SERS and investigated several spherical hybrid NPs in immersion with optical trapping. They found for multilayered dielectric-metal spherical NPs an increase of 24-fold of the SERS signal and substantially decreased noise. Another study by Xu et al. [105] looked at optical trapping for an dielectric metasurface in immersion of a Si cylinder dimer with a gap of 50 nm and a Si ring surrounding it and used fluorescence microscopy to observe the trapping process of polystyrene particles. They concluded the reduced E-field is not a problem as the lower losses of dielectrics allow higher laser intensities and show that particles up to 100 nm can be trapped with their metasurfaces. Lastly Kenworthy et al. [16] simulated in FDTD a lattice of Si dimers with a gap of 20 nm for the trapping of radius 9 nm in immersion. Before trapping average EFs of 10³ were measured, this is two orders lower than a similar dielectric metasurface in air by Černigoj et al. [15] due to the lower refractive index contrast. After they simulated optical trapping depending on the laser intensity and trapping time they found higher EFs of 10⁵ comparable with Černigoj's results for dry SERS.

3 Method

3.1 Reproduction and Convergence testing

Due to FDTDs high speed in doing simulations over a large frequency range, the decision was made to model the EM fields of the new designs with Lumerical Inc FDTD 3D electromagnetic simulation software [113]. Previous works were done in COMSOL [114] using the Finite Element Method (FEM) and slight differences between the methods is expected. Reproducing the metasurface designs in [15] and [16] in Lumerical provides a comparison between these methods, and validates the simulation parameters in Lumerical and the post-processing of the data for the calculation of the EFs. Both their designs are very similar fig 12 as [16] metasurface was optimized to provide the same resonances in water. In both designs the gold surface reflects the incident light and the spacer functions to reduce the LSPs. To achieve the same SLR [16] adjusted the unit cell dimensions according to the grating distance found in (14) which simplifies to $D = \lambda/n_2$ for the first diffracted order. Second, by optimizing the cylinder radius and height for similar Mie resonance, small adjustments were made to the shape of the cylinders.

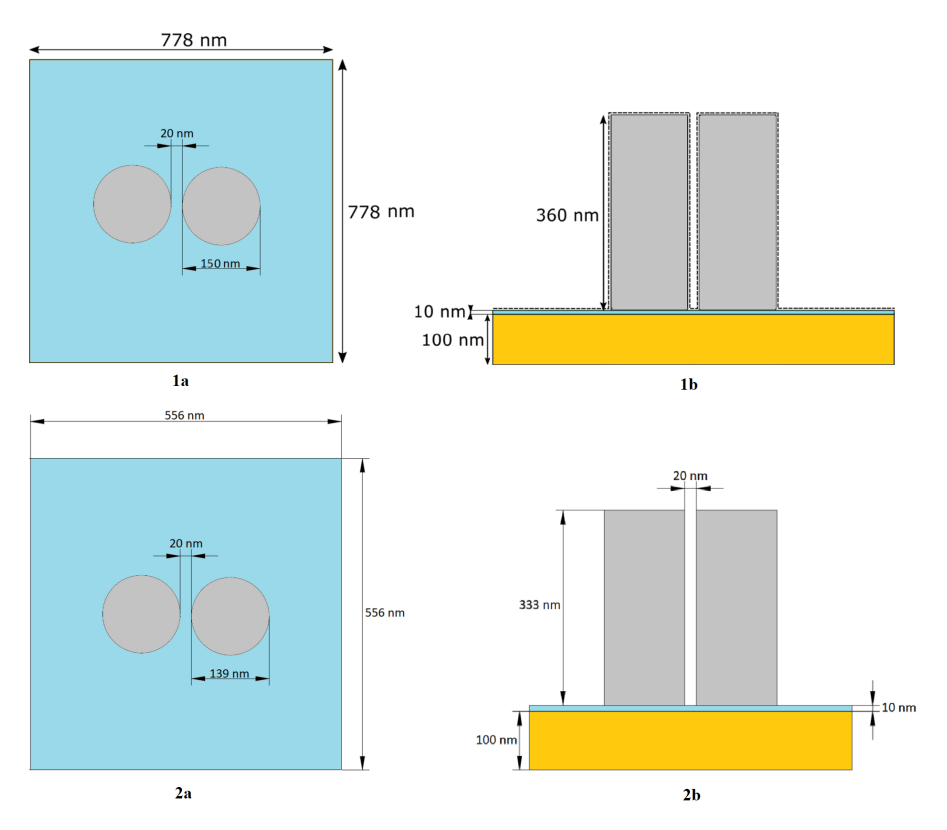


Figure 12: Sketch of [15] and [16] metasurface designs. In grey the silicon cylinders, in blue the fused quartz spacer, and in yellow the reflective gold layer. 1a: x-y cross section of [15] design, 1b: x-z cross section of [15] design, 2a: x-y cross section of [16] design, 2b: x-z cross section of [16] design.

A major difference between Lumerical FDTD and COMSOL FEM is that Lumerical FDTD only has access to a Cartesian mesh due to the Yee grid cells. A drawback is that it is less able to accurately resolve circular structures. Only reducing the mesh size is not ideal for optimization since simulation time scales with $1/D_x^4$ [102]. A finer mesh also reduces variations in field distributions. Lumerical offers multiple meshing options to better resolve interfaces between two materials. The descriptions of these methods do not fully provide an answer which method is superior. Another part of the simulation that requires attention is the PML boundary. Due to its discrete nature it might produce numerical instabilities and large reflection errors if incorrect settings are used. In most cases the convolutional or stretched PML option is sufficient and is chosen as the default option. Here a high number of PML layers improves absorbance and reduces reflections, but are more computationally expensive. Another important parameter is the distance of the PML from the metasurface. If the metasurface is too close the reflected modes from the PML interact with the metasurface producing spurious effects. Convergence testing is needed in order assess which

settings should be used for the simulations. Convergence testing is done by considering the relative error of the metric $\Delta \sigma_i$ for each *i*th value of the parameter being tested

$$\Delta \sigma_i(\lambda) = \sqrt{\frac{\int (\sigma_i(\lambda) - \sigma_{i-1}(\lambda))^2 d\lambda}{\int \sigma_i(\lambda)^2 d\lambda}}$$
 (27)

Here sigma is the metric under consideration, in the case of this research the maximum electric field (ME) and EF.

The convergence tests pointed out errors in the simulations. One key problem is that for a single broadband simulation with equally spaced frequency steps it is not able to accurately resolve high Q resonances enough such that EF converges properly. As the meshing of the simulation became finer the SLR slightly shifted due to a small change in the numeral dispersion. This resulted in a higher or lower SLR magnitude depending if the top shifted away or towards a simulation frequency point. As this top is very sharp this resulted in significant decrease of the found magnitude of the SLR. This error is squared when calculating the EF resulting in large variations between simulations. The solution is to run a second narrow band simulation after the broadband simulation localized the resonance. Then instead of wavelength steps of around 1 nm per step, values of 0.01 nm should be applied for the second simulation. It is advised to not make the narrow band range too small, because the dispersion created by the Yee grid (18) shifts the resonances for broadband simulations approximately 0.5-1 nm.

Using this new method a good mesh size could be selected for testing with the PML related parameters. These were easily kept below a convergence of 0.001 meaning the meshing is the main source of error in ME and EF. The final result for convergence testing of EF can be seen in Appendix B. Reproduction of [16] metasurface proved to be troublesome. The COMSOL files were accessible and after investigation it was concluded the meshing applied in the simulations of their final design was too coarse. Another simulation was run with finer mesh settings and compared to their results. A description of the impact on EF and a graph can be found in appendix C. Lastly, a table of important settings used in the Lumerical simulations is given in Appendix D

3.2 Exploration and optimization

The goal of the exploration is to discover new metasurface designs which have large and strong hotpots with high EF and are easier to manufacture. This can be achieved by prioritizing designs with larger gap distance, high SLRs, and smooth and high Mie resonances in the Raman shift region of the spectra. However, the magnitude of the Mie resonance plays a small role for large gaps as its decrease will make this resonance very small in comparison to the small gap designs of [15] and [16].

For the new designs the gap distance will be varied and the ME and average EF will be calculated from the spectra from excitation frequencies in the range of 750 nm to 850 nm. In addition field distributions will also be assessed through visual inspection. Enhancements more centralized within NPs will be prioritized for compatibility with optical trapping. Also the number of NPs and their position on the metasurface will be varied. Examples of this are the positioning of NPs in an array or positioning them equidistant on a circle. For these designs excitation with linear polarization will be compared with circular polarization. Excitation along the centre axis of both NPs gives the best electric field enhancement between two NPs and for circular polarization this excitation is reduced by approximately 29%. However all orientations experience this excitation equally so for the structures with more than two NPs this could produce more and larger hotspots.

The simulations require a meshing value for which convergence stabilized to a sufficiently low level to make a reasonable comparison between different designs. From graph 31 appendix B it can be observed this happens at 15 mesh cell per wavelength, but to have some margin 20 mesh cells per wavelength was used. This margin is required as the convergence of new designs not necessarily follow the convergence of [16] design. The simulations will be run on a high performance computing cluster were the results for a sweep are automatically processed through a python script. After all the sweeps are done then depending on the values found a decision needs to be made which final structures with which gap sizes will be used for optimization.

Despite the large amount of computational resources available concessions need to be made to ensure the optimization goals are achieved within reasonable time. The time scale of simulating and processing each design still ranges into a few minutes. This becomes problematic for optimizing large ranges for multiple parameters. So instead of a multi-parameter type optimization, where all

parameters are varied simultaneously and a large part of the parameter space is explored, a step wise semi-optimization scheme is done. Here from certain initial parameters a single parameter will be varied. Next the new value for this parameter is determined by picking the one with highest ME and EF. Then a sweep is done for the next parameter and this is repeated until they do not improve anymore. This process is repeated with different initial parameters if the semi-optimization yields EF values far lower than those found by [16]. The choice of the initial parameters is based on either the reproduced designs or prior optimized designs which gave sufficient enhancement. After this, the optimized structures is simulated with very fine meshing which yield the final EM and EF value for the designs. It is recognized this method is not optimal, however doing research on optimization for this type of problem and exploring more sophisticated methods is outside the scope of this thesis.

3.3 Optical trapping with new Designs

The basis of the optical trapping follows the theoretical framework discussed in the theory. The MATLAB implementation of the optical trapping algorithm of [16] has been more generalized to accommodate the types of metasurface used in this project. In addition improvements to speed up the run time are implemented and bugs were fixed. In this algorithm the particles only collide with the metasurface in the simulation reducing the complexity and computational power required significantly. The initial positions of the particles follow a uniform distribution where the last layer consisting of the remainder of the particles is stretched in order to distribute the particles as uniformly possible on this last layer. The end positions are used to calculate the EF after optical trapping

$$EF(\lambda_e) = \frac{1}{N_p} \sum_{k=0}^{N_p} \left| \frac{E(\lambda_i, \mathbf{r_k})}{E_0} \right|^2 \left| \frac{E(\lambda_s, \mathbf{r_k})}{E_0} \right|^2$$
 (28)

Depending on the field distribution of the new design, the laser intensity found in [16] might have to be slightly changed. If the laser intensity is too weak, then the field gradient of the hotspot is too weak to properly trap a particle. If the laser intensity is too high, there is a chance the particle will be trapped in a local maxima instead of the global maximum of the field. Several intensities need to be explored for each metasurface in order to allow the particles to escape local maxima and have a chance to enter the global maximum, often centred in the unit cell between NPs, where the chance to leave is much smaller due to the larger gradient field. However, if the difference between the ∇E of the centre hotspot and other local hotspots is small, it is very hard to achieve this without the reverse also happening. In this case after some time an equilibrium between these is reached and the number of particles in the centre hotspot will not, or barely, increase for longer simulation times. To measure the performance of optical trapping between different metasurfaces for 10 nm particles, times of approximately 1 ms is enough, since then most of particles are already trapped. Due to their lower speed 40 nm particles need approximately 10 times longer to reach the same state, thus 10 ms. This does not change computation time, because 10 times larger time steps are sufficient for 40 nm particles. For the final EF of optimized metasurfaces optical trapping was done 10 times longer for both particle sizes as by then the EF has converged [16]. The EF after optical trapping can be also interpreted as the average EF value found for particles released in random positions, given many particles are released in a uniformly distribution. This is can be accurate for low concentrations of small particles as its very unlike for particles to then collide.

4 Results

4.1 Multiple cylindrical structures

4.1.1 Linear vs circular polarization

As trapping is a key element in this project these structures were designed for metasurfaces in immersion. In this work, only cylinders positioned on a circle, were the radius is determined by the minimum gap between the cylinders g, were explored. First, the number of cylinders and the minimum gap in between them were varied. The parameters for cylinder height h_c , radius r_c , and x and y unit cell distances, x and y were fixed and the values found by [16] were used for these parameters. In fig 13 the x-y view of several different multi NP structures are given. For linear polarization an alignment of the electric field along x, x-polarized, is always chosen, since this is known to produce best ME and EF in the dimer case. The influence of circular polarization was also investigated. In fig 14 and 15 the resulting ME of the SLR and average EF of 2, 3 and 4 cylinder structures are given for both linear and circular polarization. In appendix E the results for 5,6,7, and 8 cylinders are given. It can be observed in fig 14 and 15 that for structures with 4 cylinders at some point no values were generated. This is due to decision to fix the unit cell size.

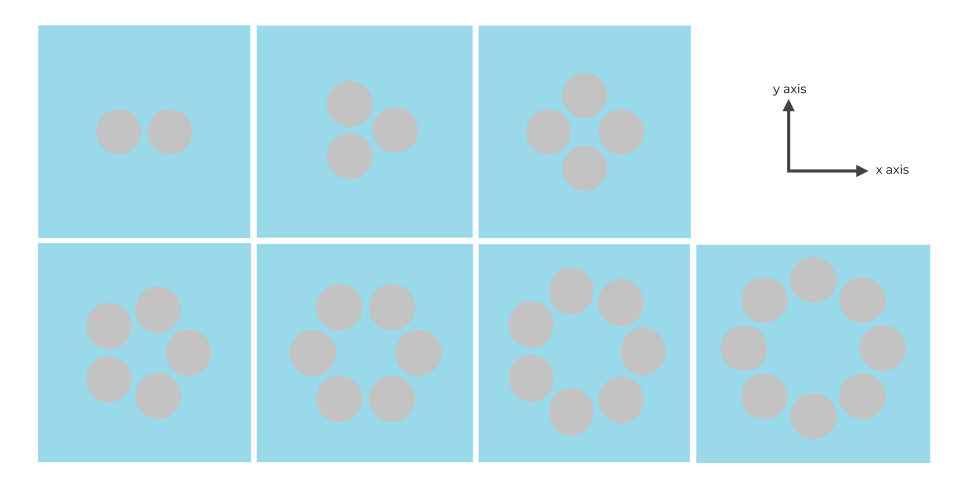


Figure 13: x-y view of different design types explored with in this case a 20 nm gap between the cylindrical NPs

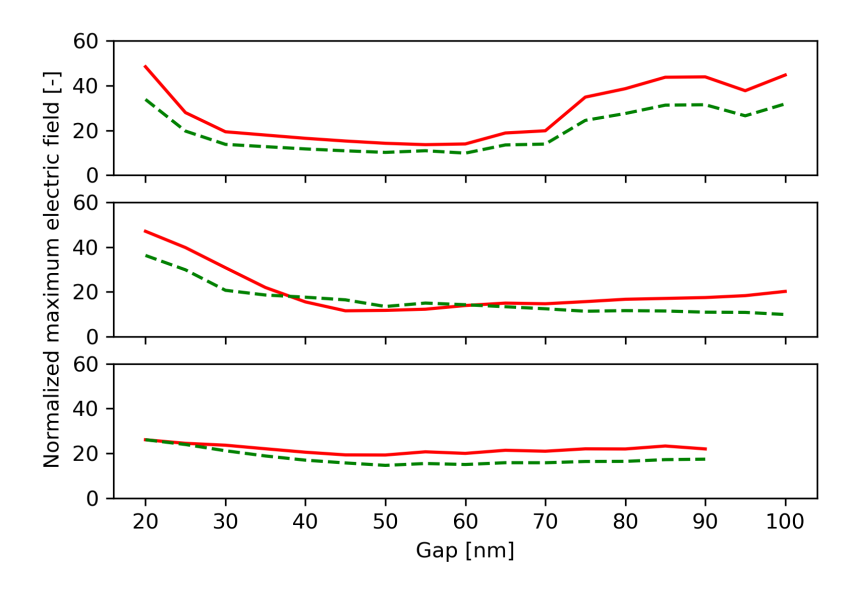


Figure 14: Normalized ME vs gap found during exploration of metasurfaces. **Red solid line**: linear polarization with electric field component in x-direction. **Green dashed line**: circular polarization. **top**: dimer, **middle**: trimer, and **bottom**: quadrumer.

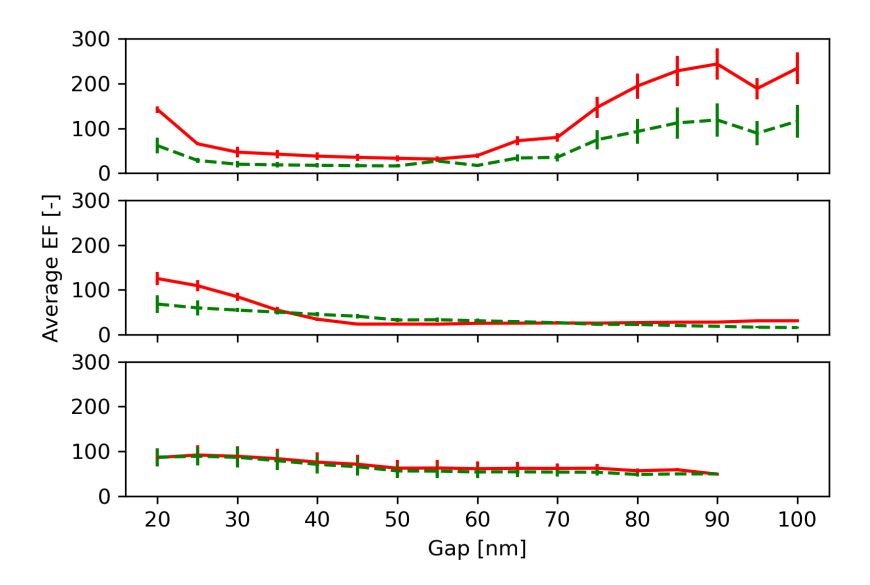


Figure 15: Average EF for all Raman shift frequencies with standard deviation vs gap found during exploration of metasurfaces. Red solid line: linear polarization. Green dashed line: circular polarization. top: dimer, middle: trimer, and bottom: quadrumer.

Linear polarization produces overall better results in the dimer case. This corresponds with theory since x-polarization gives then the best possible enhancement with Mie resonances. Due to destructive interference of the SLR resonance, the region between 30 nm and 60 nm has a magnitude that is equal to the maximum of the Mie resonance. This also explains the steady decrease of the ME as the Mie resonance magnitude decreases for larger distances between the cylinders. The ME is consistently lower, but not exactly $\frac{1}{\sqrt{2}}$ since the y-polarized electric field still produces a small electric field enhancement between the two cylinders. This resonance compensates relatively better when the magnitude of the x-polarization resonance is lower as seen with gaps from 30 nm to 70 nm. For larger gap values, beyond 70 nm gaps, large SLRs can be found and average EFs can be found that seem capable of surpassing the small gap structures were the Mie resonance plays a large role. These results indicate Dimer structures with linear polarization and large gaps can sustain large ME of SLRs and EFs.

Circular polarization does not seem to prove an advantage in most cases. An example were this is the case can be seen in the trimer for a gap in the range from 40 nm to 60 nm. In this case there is no pair of cylinders aligned with the x-polarized linear polarization. Thus it is possible for resonances from circular polarization to exceed the linear polarization. Generally, the ME found is lower for circular polarization as expected for the $\frac{1}{\sqrt{2}}$ factor. Again this is somewhat compensated by the field of the orthogonal polarization as seen by the small difference between the ME and approximately same average EF. Particularly noticeable is the very similar average EF for both polarization in the quadrumer case. The Raman shift for each gap indeed gives exactly the same average EFs for each gap distance. The fields however do differ for circular polarization were the fields are more spread out and more homogeneous within the centre and in between the cylinders as seen in fig 16. The symmetry of the quadrumer creates this phenomena since the alignment exactly correspond to the x and y unit cell axis. This makes the quadrumer interesting despite its relatively low EF. Another promising aspects is the fact particles with a diameter several times larger the gap can enter this region through the top of the quadrumer structure. This diameter d_p can be derived from the geometry of the metasurface and in the quadrumer case this is $d_p = (\sqrt{2} - 2)r_c + \sqrt{2}g$.

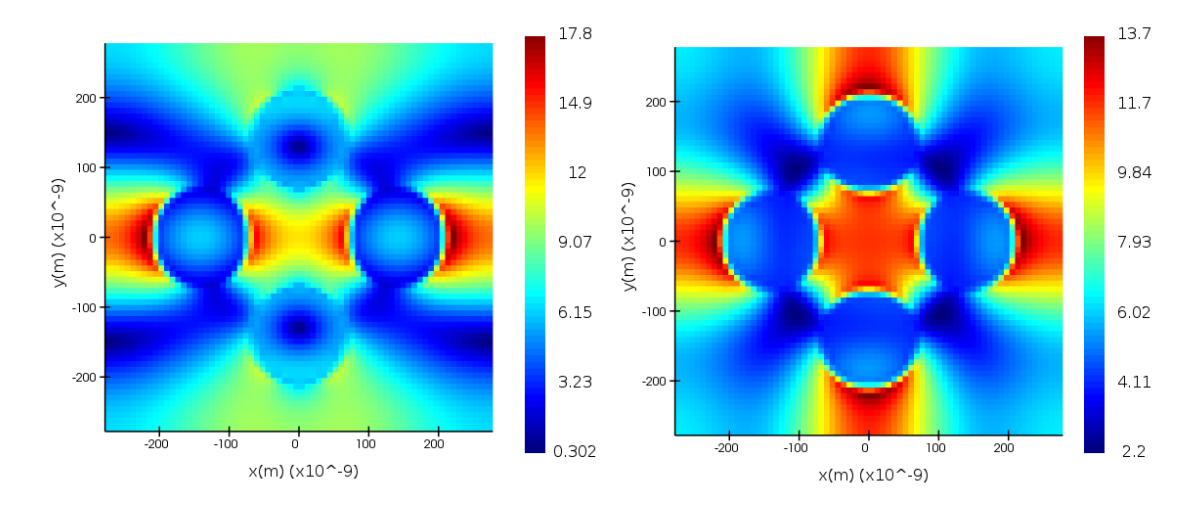


Figure 16: x-y view at 2/3 cylinder height of the normalized electric field for the unit cell of a 60 nm gap quadrumer structure for both polarizations. **Left**: linear polarization. **Right**: circular polarization.

For this reason, three quadrumer metasurfaces were optimized for gaps of 20 nm, 60 nm, and 130 nm. The resulting variable metasurface parameters are given in appendix F. Again it can be seen in fig 17 that the EF is very similar in quadrumer metasurfaces for both polarizations. The 60 nm and 130 nm quadrumer metasurface seem better capable of producing high EFs than the 20 nm quadrumer. The little bump at the end of 130 nm gap quadrumer is most likely due to a higher order SLR, but does not severly disrupt uniformity of the raman shift spectrum. In addition, they have lower gap/height ratio of 10.67 and 5.23 respectivly than the 15.75 of the 20 nm structure. However, the EFs when doing optical trapping, as seen in fig 18, show a significant improvement for the 20 nm quadrumer. Further, linear polarization performs half an order better than circular polarization for the larger gap quadrumers. The 20 nm quadrumer has stronger, but smaller hotspots. The same for the linear polarizations of the 60 nm and 130 nm quadrumers. It can be concluded that for optical trapping the higher ME found in linear polarization are more beneficial than then larger hotspot sizes found in circular polarization. It seems linear polarization is better for producing EF after optical trapping for quadrumer metasurfaces with large gaps. For smaller gaps the difference is small and both polarizations seem to have roughly equal performance. Larger gaps in quadrumers also give an additional resonance at the centre of the y boundary which decreases trapping performance of the metasurface as the mie resonance there is lower.

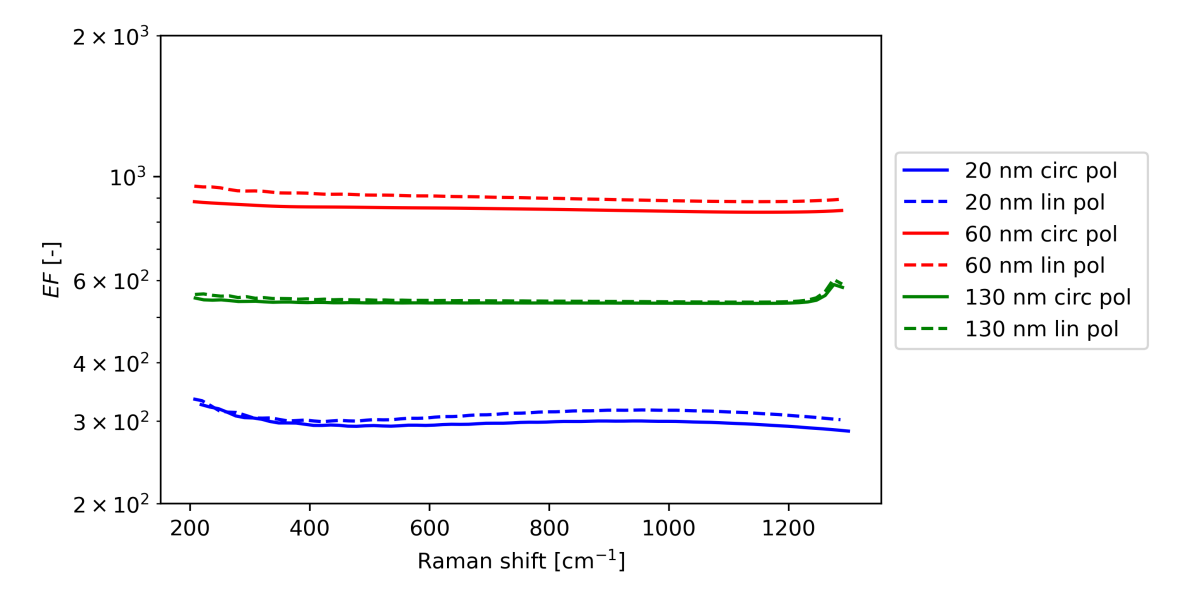


Figure 17: The EF on log scale against Raman shift for of all optimized quadrumers both polarizations

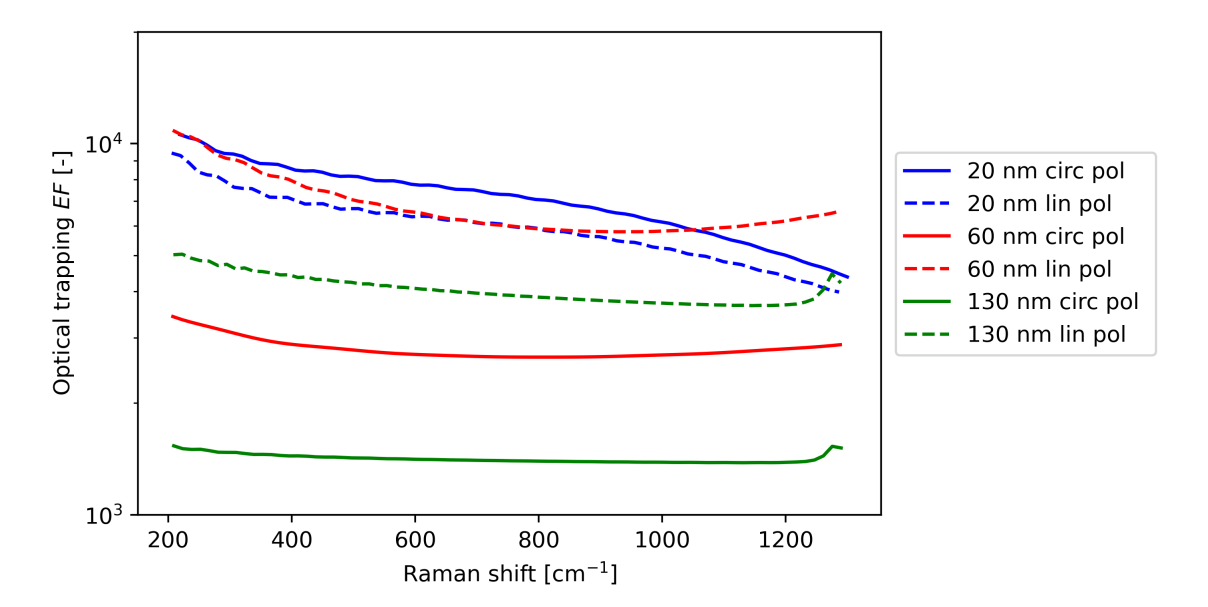


Figure 18: The optical trapping EF on log scale against Raman shift for all optimized quadrumers for 1000 particles after 1 ms of optical trapping with diameter 10 nm and both polarizations.

In fig 19 the results for optical trapping with quadrumers for larger particles with diameters of 40 nm. The overall EF diminishes for all quadrumers, because now a smaller portion of the volume of a trapped particles can enter the strongest region of the hotspots, which are always on the surface of NPs. This can be observed by comparing the trapping distribution for diameter 10 nm particles in fig 20 with the diameter 40 nm particle in fig 21 where the regions with high concentrations of trapped particles are slightly further distanced from the cylinder surfaces. For the 20 nm quadrumer it can also be seen that the particles are now unable to enter the gap between the NPs. In total, this results in an order lower performance for this metasurface and worse performance than the larger gap quadrumers. This means that for larger particles it is better to apply quadrumers with largers gaps. The decrease in linear polarization is greater than the decrease in circular polarization for the 60 nm and 130 nm quadrumers. This can be explained by the more homogeneous fields of circular polarization, thus with respect to particle size circular polarization provides more consistent EFs after trapping. However, again linear polarization gives better EFs than circular polarization and for this reason the rest of the quadrumer performance compared with other metasurfaces will have only linear polarization.

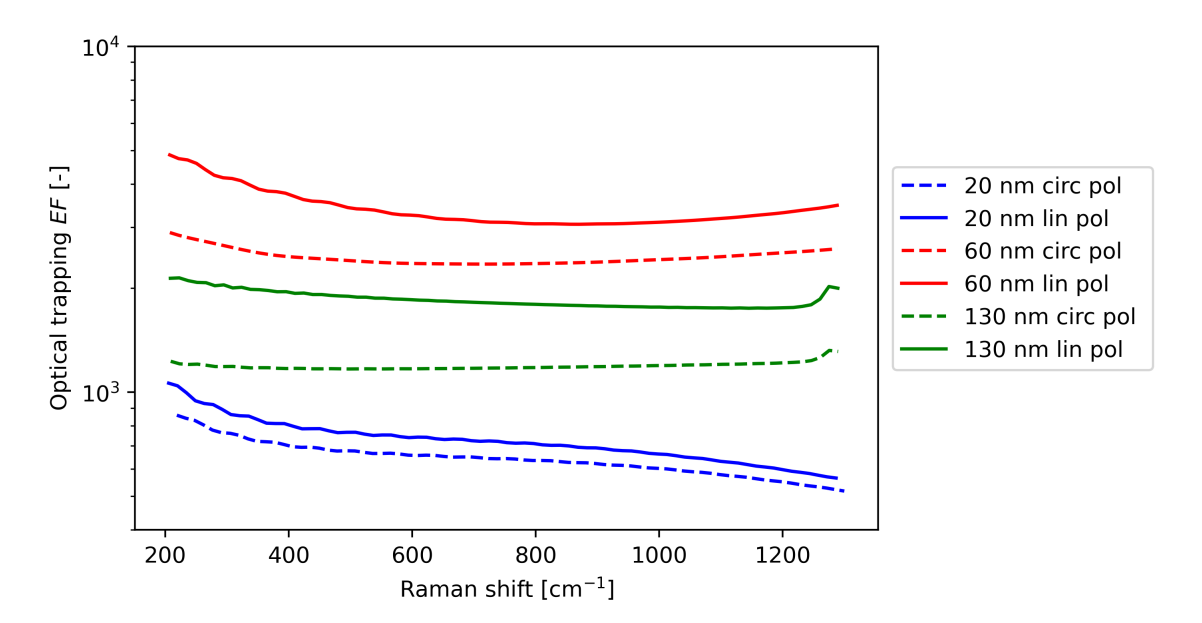


Figure 19: The optical trapping EF on log scale against Raman shift for all optimized quadrumers for 1000 particles after 10 ms of optical trapping with diameter 40 nm and both polarizations.

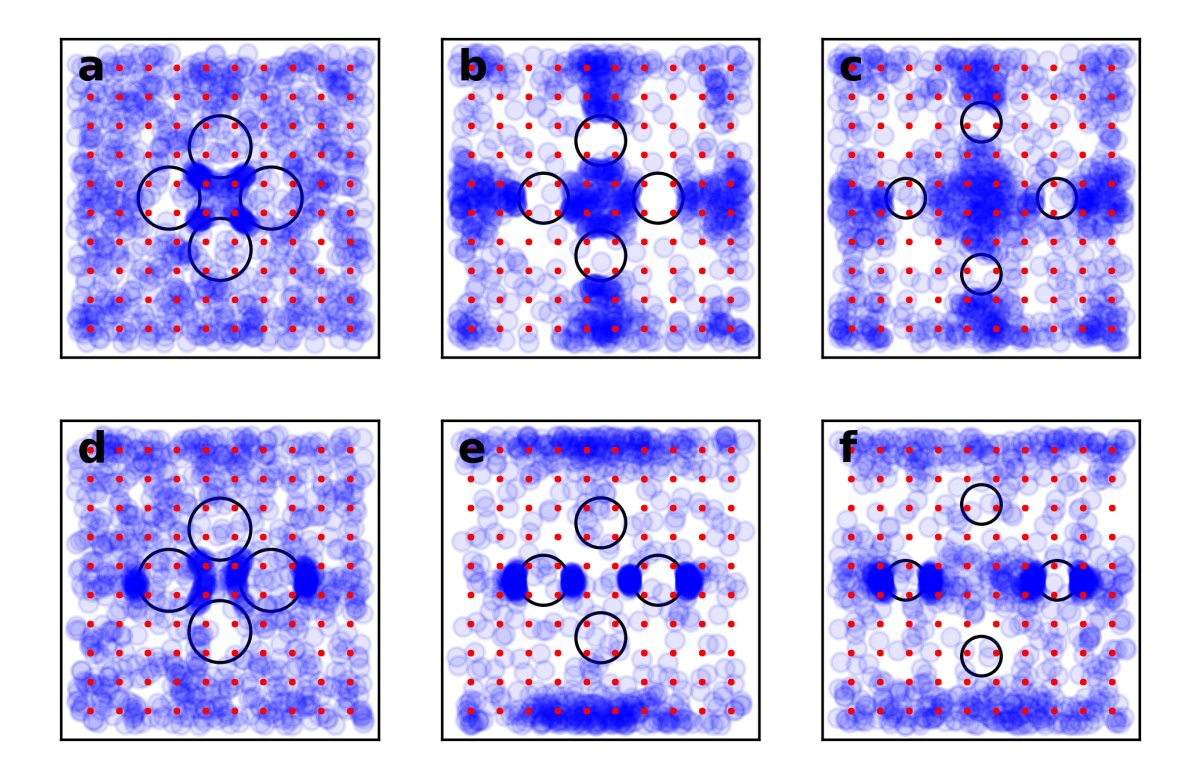


Figure 20: x-y distributions of 1000 particles released in the free volume for diameter 10 nm particles after 10 ms of optical trapping in the unit cell of all quadrumer metasurfaces. All unit cells of the quadrumers have size x-y dimensions of 556 nm by 556 nm. The solid red dots are the particles initial positions on the x-y cross-section. The blue semi-transpart circles give the end positions of the particles. a: 20 nm quadrumer circular polarization. b: 60 nm quadrumer circular polarization. c: 130 nm quadrumer circular polarization. d: 20 nm quadrumer linear polarization. f: 130 nm quadrumer linear polarization.

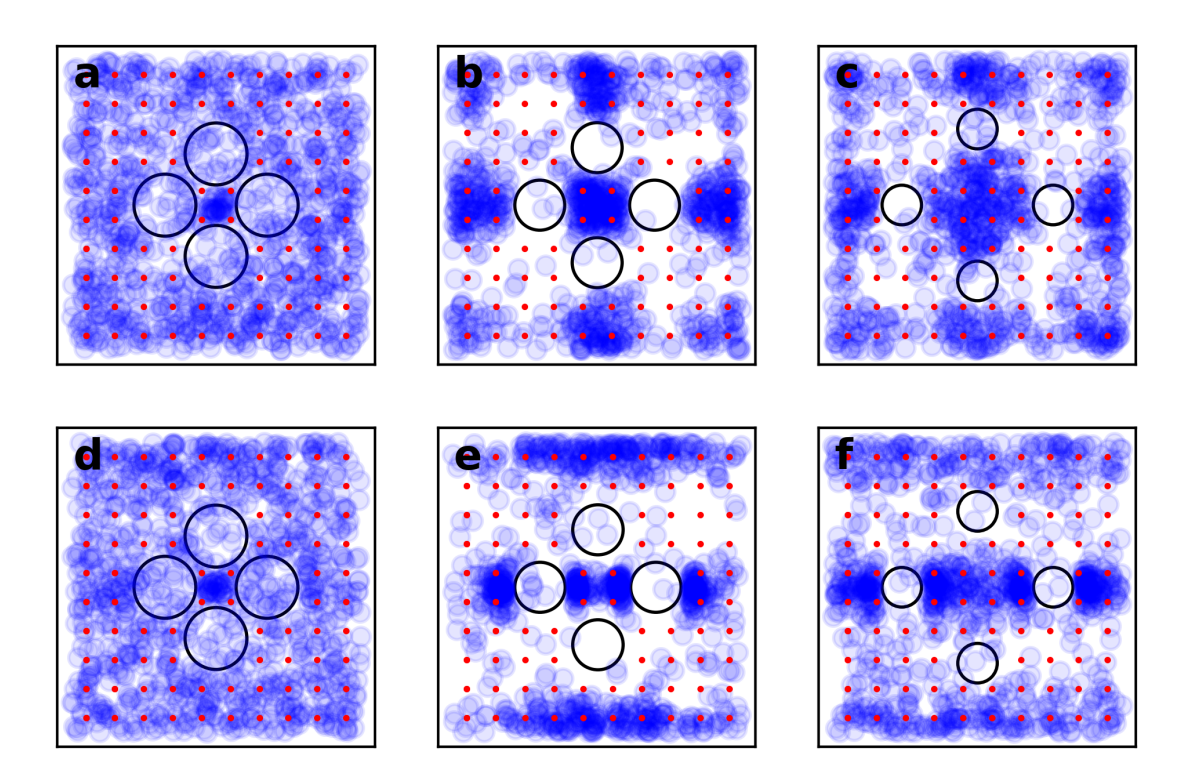


Figure 21: x-y distributions of 1000 particles released in the free volume for diameter 10 nm particles after 10 ms of optical trapping in the unit cell of quadrumer metasurfaces. All unit cells of the quadrumers have size x-y dimensions of 556 nm by 556 nm. The blue semi-transpart circles give the end positions of the particles. a: 20 nm quadrumer circular polarization. a: 20 nm quadrumer circular polarization. b: 60 nm quadrumer circular polarization. c: 130 nm quadrumer circular polarization. d: 20 nm quadrumer linear polarization. e: 60nm quadrumer linear polarization. f: 130 nm quadrumer linear polarization.

4.1.2 Dimer vs quadrumer

A comparison is done between the dimer and quadrumer metasurfaces. The 20 nm quadrumer is left out of this comparison, because of its high height/gap ratio and its weak EFs for larger particles. In fig 22 the upward curvature of the new 20 nm dimer, an optimized reference metasurface to achieve EFs as reported by [16], which results from a resonance peak at the very end of the Raman shift. Ideally this would not be present, as a large uniform Raman shift enhancement is desired for all metasurfaces, however this can be ignored as this is a quick reference structure and for most analytes the relevant peaks in the Raman spectrum are below the value of $1000 \ cm^{-1}$.

It can be seen from fig 22 that the 130 nm dimer has a superior EF of 2000 twice has high as the EF of the reference 20 nm dimer. The 60 nm quadrumer has the same performance as the 20 nm dimer and the worst is the 130 nm dimer with an EF of 600. After trapping the 20 nm dimer achieves an EF close to 10^6 as seen in fig 23. However, this is the least manufacturable metasurface with a height/gap ratio of 25. Second comes the 130 nm dimer which has far better manufacturability with a height/gap ratio of approximately 7. but lower optical trapping EF of about 5×10^4 . In addition, the 130 nm dimer has an additional hotspot at the y unit cell boundary of approximately equal magnitude as in the center. This limits the potential of optical trapping for this metasurface as a large percentage of the particles will always be trapped in this region instead of in the center where the Raman shift enhancement is higher. This is also the case for the 60 nm and 130 nm quadrumers.

In the case of diameter 40 nm particles the 130 nm gap dimer structure is superior to 20 nm gap dimer as seen in fig 24. This is due to the fact the particles can not enter the center hotspot region anymore also seen in fig 36a. Overall for larger particles the best EF attainable for these metasurfaces after trapping is about 10^4 . The 130 nm dimer comes out as superior in both case, however it does not achieve the 10^5 EF as reported by [16]. Two other options to achieve this were explored.

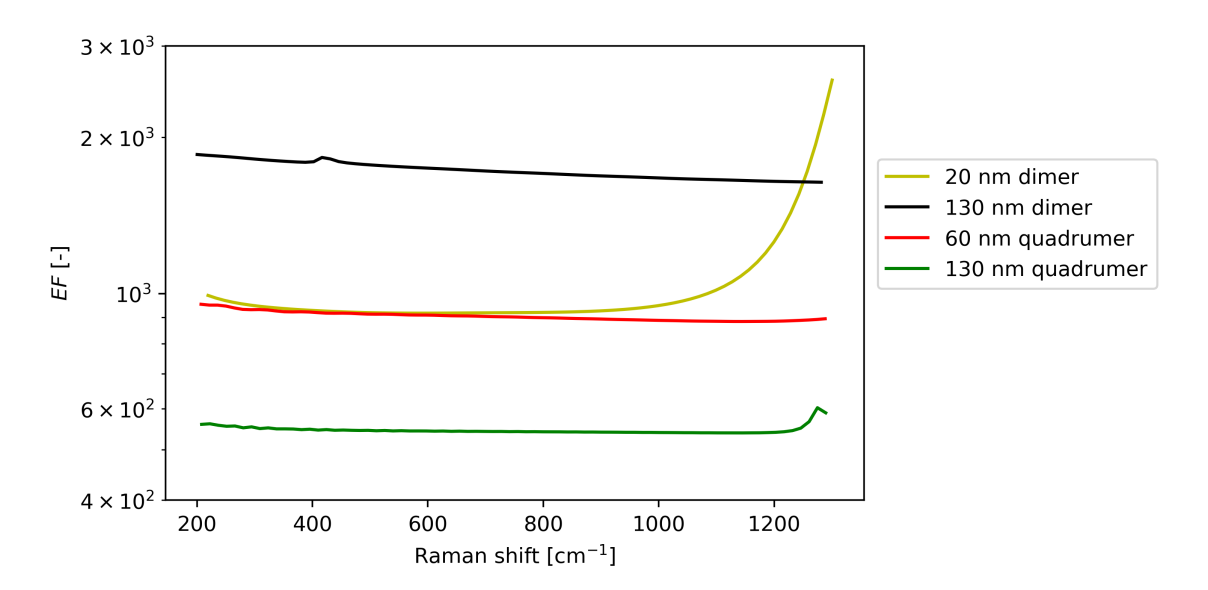


Figure 22: The EF on log scale against Raman shift for optimized dimers and quadrumers excited with linear polarization.

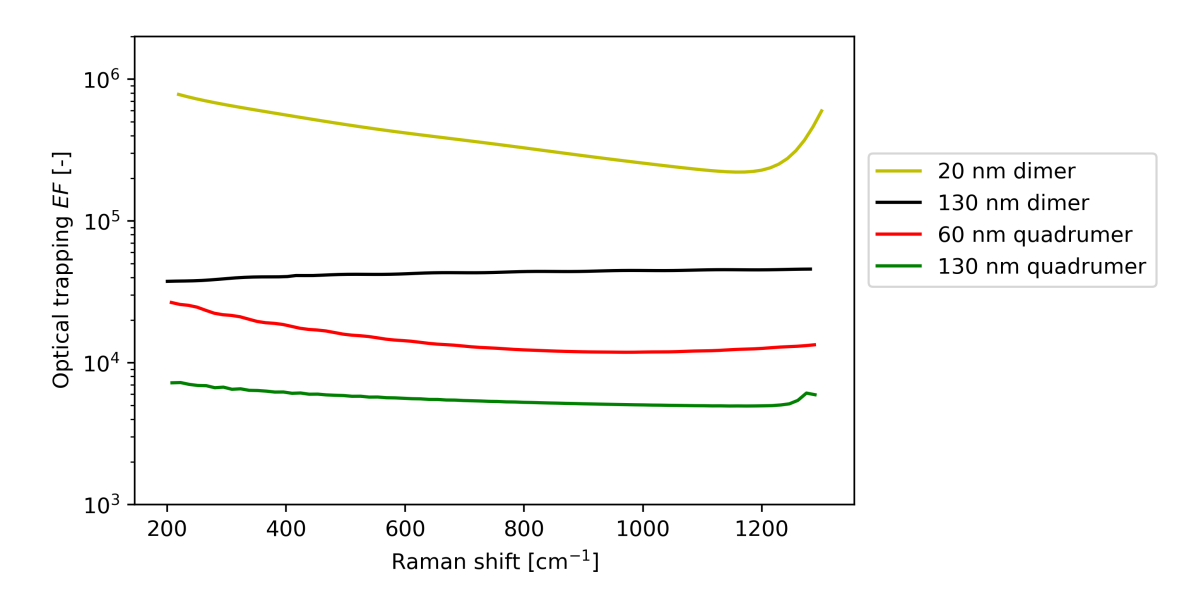


Figure 23: The optical trapping EF on log scale against Raman shift after 10 ms of trapping of 1000 particles with a diameter of 10 nm for optimized dimers and quadrumers excited with linear polarization.

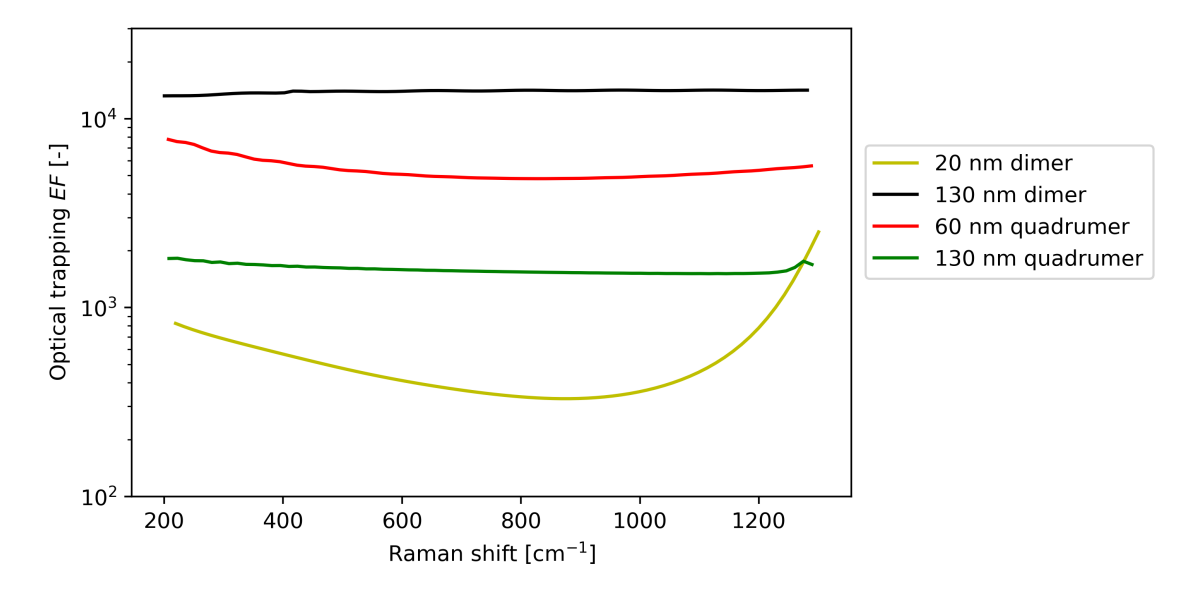


Figure 24: The optical trapping EF on log scale against Raman shift after 100 ms of trapping of 1000 particles with a diameter of 40 nm for optimized dimers and quadrumers excited with linear polarization.

4.2 Trapping schemes

By changing the laser intensity during optical trapping the strength of the optical trapping can be changed. This could possible be exploited to improve EF and for this reason two new schemes for optical trapping were investigated. Scheme 1 where after trapping for 9ms the laser intensity is increased 10 fold for 1 ms. This increases the dielectrophoretic force and should result in particles more "tightly" trapped in the region of highest electric field. For scheme 2 the opposite is done where first is trapped for 1 ms with the 10 fold increased laser intensity and then for 9ms with the default laser intensity. This should trap the particles to the hotspot regions sooner thus could result in more favorable initial positions for more particles before they move more randomly around with the lower laser intensity.

In fig 25 the EF is given for application of both schemes on the 130 nm dimer. Scheme 1 indeed provides a better EF than the 10 ms with the default laser intensity. The effect on the distribution of particles can be seen in fig 26. Scheme 2 does not provide any improvement. This is possibly due to the fact that the particles close to the hotspots would most likely to be trapped at the local hotspots anyway and thus trapping them earlier makes virtually no difference. The effects of scheme 1 on optical trapping is more clearly visible in fig 26.

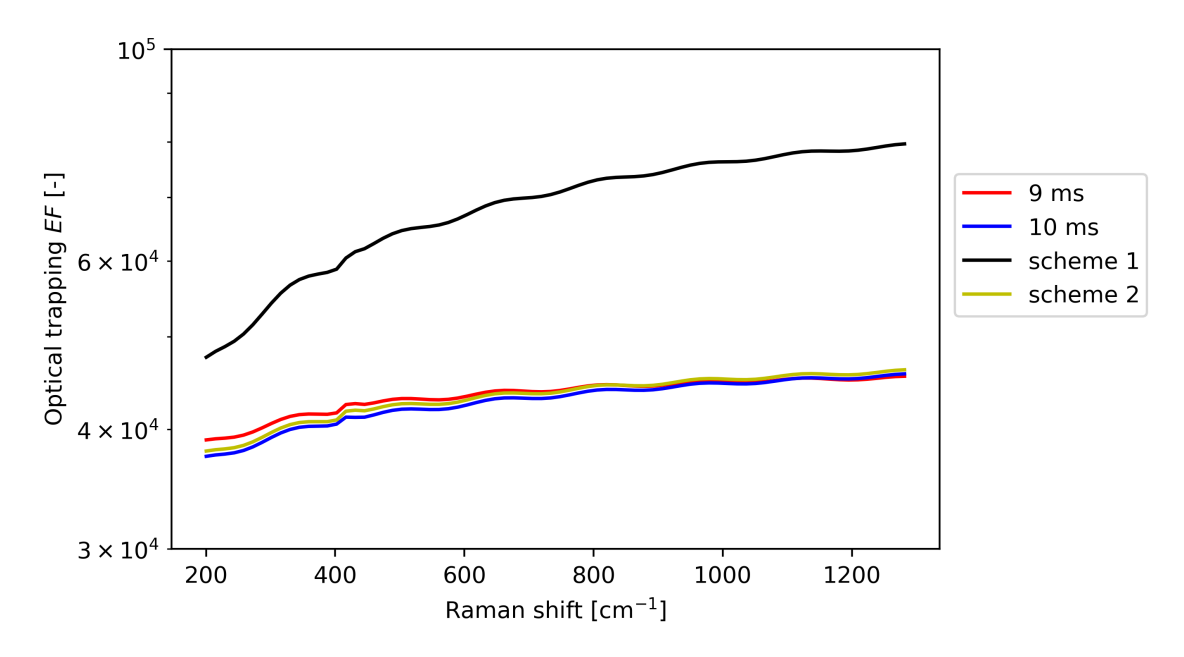


Figure 25: The optical trapping EF on log scale against Raman shift after 9 ms and 10 ms and both schemes of trapping of 1000 particles with a diameter of 10 nm for 130 nm dimer excited with linear polarization.

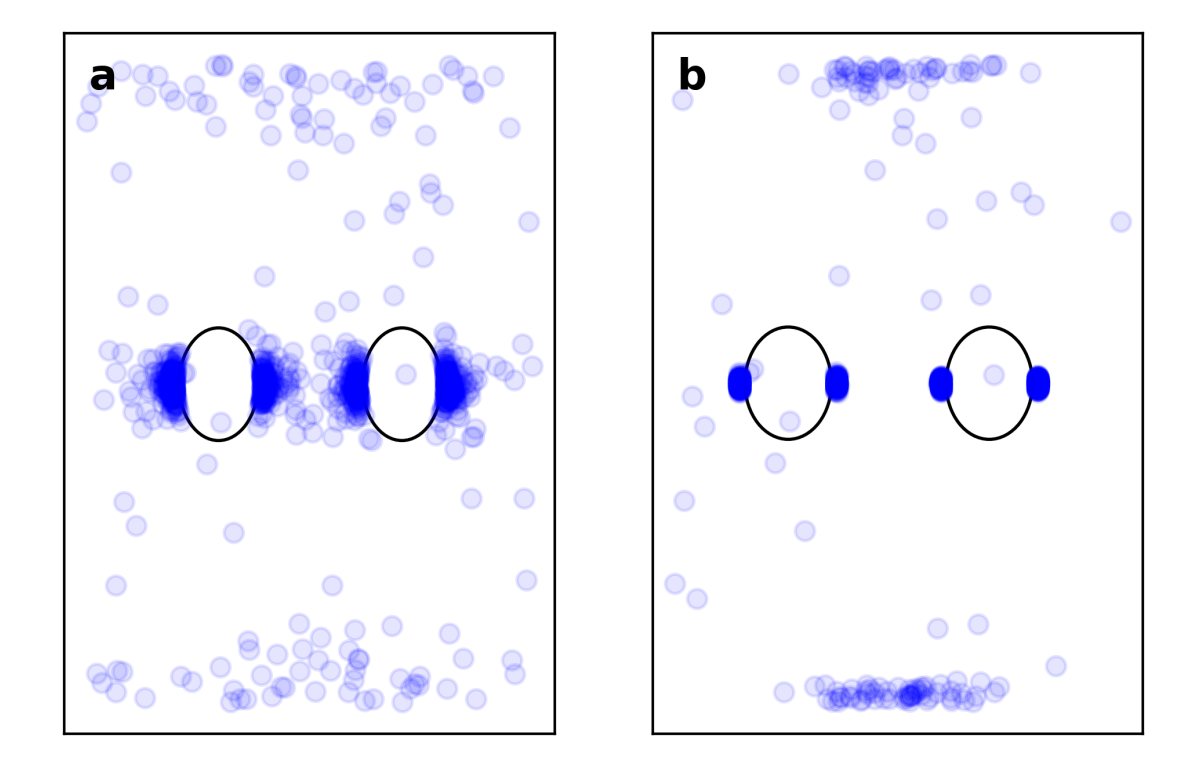


Figure 26: X-y distributions of 1000 particles released in the free volume after optical trapping with diameter 10 nm for the unit cell of 130 nm gap dimer excited with linear polarization. Both unit cells of the dimers have size of 556 nm by 556 nm. The blue semi-transpart circles given the end position. a trapping for 10 ms. b trapping for scheme 1.

4.3 Line metasurface

In order to address the issue of the local hotspots on the sides of the cylinders another type of design was optimized. As shown by [71], changing the periodicity in the x direction does not greatly change the magnitude of SLRs, so for this new metasurface the distance across the unit cell between cylinders is changed to the gap length. This change now results identical fields at the sides of the cylinders and the new design has a unit cell which consists of only one cylinder. This design

has an increase in hotspot density as more cylinders are now densely packed in the x-direction. This does not address any other non desired hotspots as the large hotspot at the y-borders of the unit cell in the 130 nm dimer and 60 and 130 quadrumers, but could improve performance overall. Ideally only the centre resonance between the cylinders should have a high ME so all particles would effectively be trapped in the best region given enough time. In the worst case, the particles would move less favorable initial positions due to being non centered maxima as seem

In fig 27 it can be seen this new design has similar performance to the 20 nm dimer. After optical trapping it has an EF of slightly less than 10^5 as seen in fig 28, but can be increased to about 10^5 with trapping scheme 1. In addition, it has the best performance for trapping larger particles and the decrease in EF for trapping larger particles is also smaller. The height/gap ratio of 13 of the line metasurface is smaller than the 16 of the 20 nm gap dimer. The line metasurface has 10^5 EF after optical trapping if scheme 1 is used, capable of trapping larger particles with slightly decreased EF, and has better manufacturability than the reference.

However, for high analyte concentrations the results of fig 28 are not realisable, since a lot of particles partially overlap. To remedy this, the overlapping particles are removed which gives EFs seen in fig 29. As only a few particles fit in the hotspot region of the 20 nm dimer the EF drops with one order for 10 nm particles. For the 60 nm line metasurface it seems a lot of particles are also in the same region causing a similar drop of EF. The EF of the 130 nm dimer drops the least indicating less overlap in the hotspot regions. Optical trapping scheme shows significant decreases for both metasurfaces due to the stronger trapping in hotspot regions. From this, the improvement of EF for the line metasurface over the 130 nm dimer seems small. When considering the larger gap and better manufacturability of the 130 nm dimer better with its height/gap ratio of 7, it seems the better design despite its slightly lower EF.

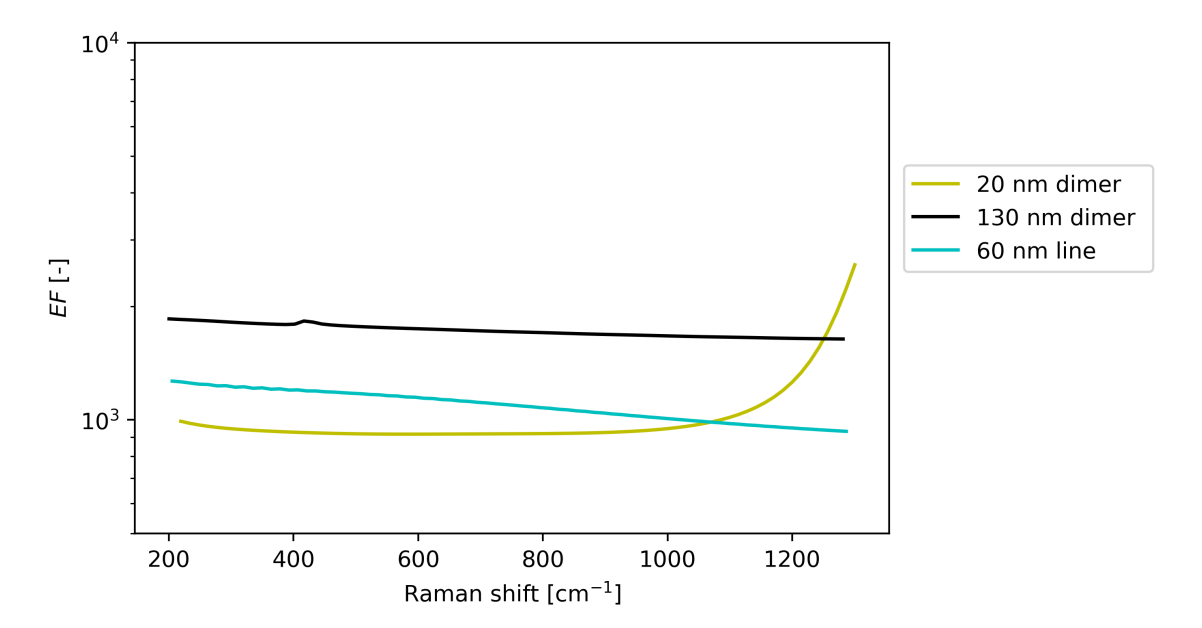


Figure 27: The EF on log scale against Raman shift for optimized line metasurface and dimers excited with linear polarization.

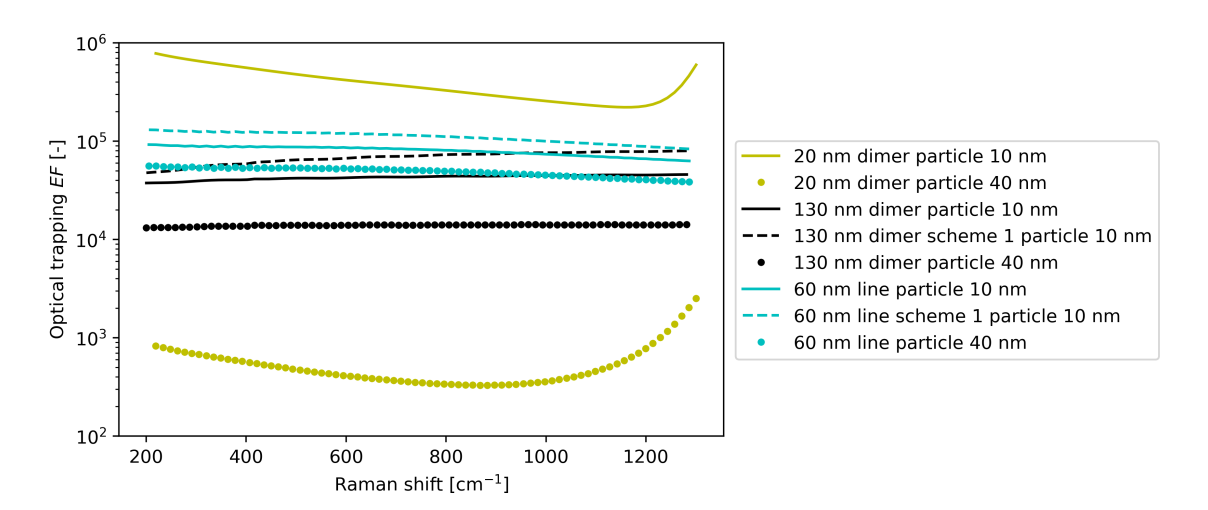


Figure 28: The optical trapping EF on log scale against Raman shift for with and without scheme 1 of trapping of 1000 particles with a diameter of 10 nm and 40 nm for line and dimer metasurfaces excited with linear polarization.

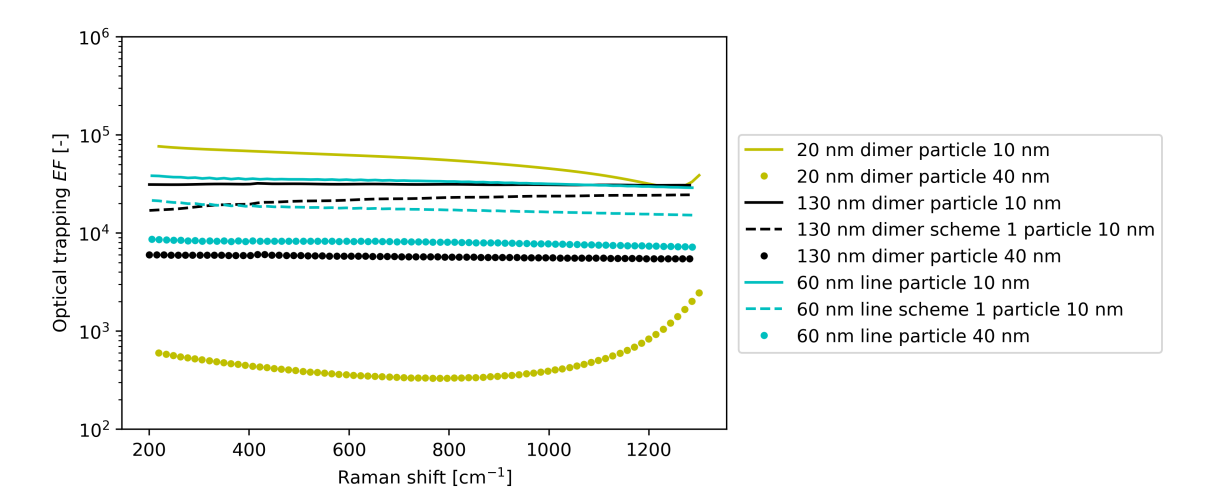


Figure 29: The optical trapping EF on log scale against Raman shift for with and without scheme 1 of trapping of 1000 particles with a diameter of 10 nm and 40 nm for line and dimer metasurfaces excited with linear polarization without particle overlap.

5 Discussion

Circular polarization does not give an advantage at producing high EF. The larger hotspots found for the quadrumers with circular polarization did however seem able to trap slightly more particles in the center region. Therefore, for trapping purposes only circular polarization can have merit. Adding more cylinders does not seem to be able to compensate for the larger gap sizes. Generally, increasing the gap decreases the raman shift enhancement due to lower Mie resonances. From the results can be concluded that for metasurfaces in immersion with an height/gap ratio of 10 between NPs, in a 750 nm to 950 nm wavelength range, and gaps larger than 20 nm EF of about 10^3 were still found. This is due to the larger region of excitation field enhancement. This reflects what is found in literature. However, with the decaying Mie resonance much higher values of EF without exploiting other resonances or methods seems improbable.

For low concentrations, optical trapping EFs of 10^5 can still be achieved with larger gaps as was reported in [16]. Values of between 10^4 and 10^5 can be expected for larger gap metasurfaces. All while these new large gap metasurfaces have a better height/gap ratio between 7 and 13 than the 20 dimer design with a ratio of 28.22 and can, due to the larger gap, house more and larger particles. For larger particles the EF will generally decrease to values between 10^3 and 10^4 , with as an exception the $5x10^4$ of the line metasurface, because the larger particle diameter results in a smaller part of the particle to be in the region of strongest enhancement. For high concentrations, EFs for larger and smaller particles can be expected to be 2 times lower, due to the fact only a few particles can be present in the regions of best enhancement. However, several simplifications and assumptions, due to time constraints and the many parameters involved, in the methods, models, and metrics affects the exploration for new designs and reported EF.

During exploration of new structures only fixed geometries for individual NPs were considered. By also varying in height and radius a larger part of the parameter space could have been explored and a better impression of the potential of the multi cylinder structures could have been the result. Running simulations with circular polarization results in 2-4 times longer simulation times for a single design than when using linear polarization. If initial exploration was done with only linear polarization, then sweeps in height and radius could have been feasible. A similar method as in the semi-optimization could then be used to find the height and radius that produced better EF for a N cylinder configuration with a certain gap size.

The ME as a metric does not tell much about the size of the resonance. While EF does do this to some degree it also takes the enhancement within different hotspot regions which is undesired from an optical trapping point of view. An increase in E in the centre region should be accompanied by a homogeneous increase in the other regions to prevent other strong field gradients to arise and particles being trapped there. Distributing the simulation region in several sections and calculating for each the ME and EF could have given a better impression of the overall enhancements found in the design. Even still, limitations of modelling in Lumerical and the optical trapping algorithm provides challenges in accurately predicting EF.

The cylinders would not have identical shapes as a results of inaccuracies in manufacturing. In addition, they would not be perfectly cylindrical. The latter is however indirectly taken into account to some degree during discretization of the metasurface whilst meshing. Secondly, the gap distances would also have some level of variation during manufacturing. Thus, EF could be severely reduced because the unit cells would not be identical and would produce lower magnitude SLRs. Further it is assumed the NPs are perfectly homogeneous were in reality this is not the case. The only way to gain an idea how the metasurface performs for perturbed shapes is by simulating these. However for perturbations between different unit cells this can become very computationally intensive as no periodicity can be used to simulate the metasurface.

The optical trapping as currently modelled is not accurate for simulating high concentrations. In the model the particles do not interact/collide with each other. This results in a part of the interactions not being taken into account. Worse, the particles can overlap completely in position and therefore too many particles occupy the hotspot region than is physically possible. This results in an overestimation of the EF after optical trapping. By removing the overlapping particles a physically realisable estimate can be achieved, but in reality they instead would form an agglomerate at the hotspot region which would at some point be completely saturated. This means the possible advantage of being able to house more particles in the gap region due to the larger gap distance is not properly explored yet. Further, the particles in this model have a refractive index of about 1.6 which is higher than the approximately 1.3 of water and thus affects the electric

field. The lower refractive index contrast would possibly result in a lower magnitude SLRs and Mie resonances. Both problems could be overcome by simulating the particle-particles collisions and regularly update the field due to the new positions of the particles in the immersion. However this would drastically increase the simulation time, because particles can not be computed parallel and adds numerous more EM simulations. In addition, EM simulations using periodic boundary conditions would introduce error as the particles have in reality different positions in each unit cell. A possible simplification could be to do predictions on average particles positions during optical trapping on certain intervals and simulating those regions with altered refractive index with the volume average of the water and particles.

6 Conclusion

In previous works the gaps between the NPs of the metasurfaces were too small and did not give good manufactureability and did not allow analytes larger than 20 nm to enter the regions of strongest enhancement. New designs and approaches were explored to maintain at least similar EF while increasing the gap size between NPs. These new designs focused on stronger and larger hotspots of SLRs to compensate for the lower Mie resonances due to larger gap distances while also prioritizing uniform Raman shift enhancement.

One of these new designs consists of quadrumers with gaps of 20 nm, 60 nm and 130 nm excited with both linear and as a new approach circular polarization. Exciting with circular polarization generally yielded lower EFs after optical trapping, because of its lower magnitude hotspots. Quadrumers did not have better EF or significantly better manufacturability than a newly designed 130 nm dimer. From this it seems quadrumers are not interesting for SERS. However, different cylinder shape parameters, unit cell dimensions, and excitation frequency ranges should be investigated before conclusive statements can be made.

A new promising approach is proposed for optical trapping were the laser intensity near the end of optical trapping is increased to force the particles closer to location of highest magnitude. This in combination with the new 60 nm gap line metesurface design with unit cell consisting of single cylinders but with different length for the x and y-axis to tackle the problem of the local hotspots at the sides of the cylinders, inhibiting optical trapping performance in previous works, resulted in similar EFs of order 10⁵ and 10⁴ after optical trapping for 10 nm and 40 nm particles respectively for low concentrations. This makes this new design a promising candidate for dielectric SERS with larger particles using optical trapping. Future work should investigate if SLRs can be further improved for this design to enable better EFs after optical trapping.

This new metasurface designs could be tuned to enable use for larger analytes such as SARS-COV-2. However, it seems the limitations of the EM simulations and the optical trapping algorithm make it hard to determine which EFs are truly realisable, especially for high concentrations of analyte, for these dielectric metasurfaces in immersion. Besides this, a large number of possible metasurface designs remain unexplored as simulations with circular polarization created additional time constraints. Future work should focus on exploring alternate metrics and optimization methods for searching new metasurface designs with stronger resonances. Until then, no conclusion can be made whether dry SERS or immersion with optical trapping for these metasurfaces in SERS has superior EFs.

References

- [1] Xueping Chen et al. "Label-free techniques for laboratory medicine applications". In: Frontiers in Laboratory Medicine 1.2 (2017), pp. 82-85. ISSN: 2542-3649. DOI: https://doi.org/10.1016/j.flm.2017.06.003. URL: https://www.sciencedirect.com/science/article/pii/S2542364917300638.
- [2] Linda J. Carter et al. "Assay Techniques and Test Development for COVID-19 Diagnosis". In: ACS Central Science 6.5 (Apr. 2020), pp. 591-605. DOI: 10.1021/acscentsci.0c00501. URL: https://doi.org/10.1021/acscentsci.0c00501.
- [3] Richard L. McCreery. Raman Spectroscopy for Chemical Analysis. John Wiley & Sons, Inc., Sept. 2000. DOI: 10.1002/0471721646. URL: https://doi.org/10.1002/0471721646.
- [4] Jeanette G Grasselli and Bernard J Bulkin. Analytical Raman spectroscopy / edited by Jeanette G. Grasselli and Bernard J. Bulkin. eng. Chemical analysis; v. 114. New York: Wiley, 1991. ISBN: 0471519553.
- [5] J.M. Chalmers. Spectroscopy in Process Analysis. Sheffield analytical chemistry. Sheffield Academic Press, 2000. ISBN: 9781841270401. URL: https://books.google.nl/books?id=GefmwAEACAAJ.
- [6] D.B. Chase and J.F. Rabolt. Fourier Transform Raman Spectroscopy: From Concept to Experiment. Academic Press, 1994. ISBN: 9780121694302. URL: https://books.google.nl/books?id=Tn53QgAACAAJ.
- [7] M.J. Pelletier. Analytical Applications of Raman Spectroscopy. Wiley, 1999. ISBN: 9780632053056. URL: https://books.google.nl/books?id=R-GhC%5C_pdIC.
- [8] David L. Jeanmaire and Richard P. Van Duyne. "Surface raman spectroelectrochemistry: Part I. Heterocyclic, aromatic, and aliphatic amines adsorbed on the anodized silver electrode". In: Journal of Electroanalytical Chemistry and Interfacial Electrochemistry 84.1 (1977), pp. 1-20. ISSN: 0022-0728. DOI: https://doi.org/10.1016/S0022-0728(77)80224-6. URL: https://www.sciencedirect.com/science/article/pii/S0022072877802246.
- E. C. Le Ru et al. "Surface Enhanced Raman Scattering Enhancement Factors: A Comprehensive Study".
 In: The Journal of Physical Chemistry C 111.37 (Sept. 2007), pp. 13794–13803. ISSN: 1932-7447. DOI: 10. 1021/jp0687908. URL: https://doi.org/10.1021/jp0687908.
- [10] Marc Vendrell et al. "Surface-enhanced Raman scattering in cancer detection and imaging". In: Trends in Biotechnology 31.4 (2013), pp. 249-257. ISSN: 0167-7799. DOI: https://doi.org/10.1016/j.tibtech.2013. 01.013. URL: https://www.sciencedirect.com/science/article/pii/S0167779913000267.
- [11] Lucas A. Lane, Ximei Qian, and Shuming Nie. "SERS Nanoparticles in Medicine: From Label-Free Detection to Spectroscopic Tagging". In: *Chemical Reviews* 115.19 (Aug. 2015), pp. 10489–10529. DOI: 10.1021/acs.chemrev.5b00265. URL: https://doi.org/10.1021/acs.chemrev.5b00265.
- [12] D. Cialla-May et al. "Recent progress in surface-enhanced Raman spectroscopy for biological and biomedical applications: from cells to clinics". In: *Chemical Society Reviews* 46.13 (2017), pp. 3945–3961. DOI: 10.1039/c7cs00172j. URL: https://doi.org/10.1039/c7cs00172j.
- [13] Zhuyuan Wang et al. "SERS-Activated Platforms for Immunoassay: Probes, Encoding Methods, and Applications". In: Chemical Reviews 117.12 (May 2017), pp. 7910-7963. DOI: 10.1021/acs.chemrev.7b00027. URL: https://doi.org/10.1021/acs.chemrev.7b00027.
- [14] Cheng Zong et al. "Surface-Enhanced Raman Spectroscopy for Bioanalysis: Reliability and Challenges". In: Chemical Reviews 118.10 (2018). PMID: 29638112, pp. 4946-4980. DOI: 10.1021/acs.chemrev.7b00668. eprint: https://doi.org/10.1021/acs.chemrev.7b00668. URL: https://doi.org/10.1021/acs.chemrev.7b00668
- [15] Jernej Černigoj et al. "Lattice Resonances and Local Field Enhancement in Array of Dielectric Dimers for Surface Enhanced Raman Spectroscopy". In: Scientific Reports 8.1 (Oct. 2018), p. 15706. ISSN: 2045-2322. DOI: 10.1038/s41598-018-33941-7. URL: https://doi.org/10.1038/s41598-018-33941-7.
- [16] Cameron F. Kenworthy et al. "Using the near field optical trapping effect of a dielectric metasurface to improve SERS enhancement for virus detection". In: Scientific Reports 11.1 (Mar. 2021). DOI: 10.1038/ s41598-021-85965-1. URL: https://doi.org/10.1038/s41598-021-85965-1.
- [17] Eric Le Ru, Le Ru Eric, and Pablo Etchegoin. *Principles of surface-enhanced Raman spectroscopy*. Elsevier Science & Technology, Nov. 2008.
- [18] Kenneth B. Crozier et al. "Plasmonics for Surface Enhanced Raman Scattering: Nanoantennas for Single Molecules". In: *IEEE Journal of Selected Topics in Quantum Electronics* 20.3 (2014), pp. 152–162. DOI: 10.1109/JSTQE.2013.2282257.
- [19] L.G. Guimarães and H.M. Nussenzveig. "Theory of Mie resonances and ripple fluctuations". In: Optics Communications 89.5 (1992), pp. 363-369. ISSN: 0030-4018. DOI: https://doi.org/10.1016/0030-4018(92) 90540-8. URL: https://www.sciencedirect.com/science/article/pii/0030401892905408.
- [20] E.C. Le Ru and P.G. Etchegoin. "Rigorous justification of the |E|4 enhancement factor in Surface Enhanced Raman Spectroscopy". In: Chemical Physics Letters 423.1 (2006), pp. 63-66. ISSN: 0009-2614. DOI: https://doi.org/10.1016/j.cplett.2006.03.042. URL: https://www.sciencedirect.com/science/article/pii/S0009261406003642.
- [21] Elena Yakubovskaya et al. "Tear Down the Fluorescent Curtain: A New Fluorescence Suppression Method for Raman Microspectroscopic Analyses". In: Scientific Reports 9.1 (Oct. 2019), p. 15785. ISSN: 2045-2322. DOI: 10.1038/s41598-019-52321-3. URL: https://doi.org/10.1038/s41598-019-52321-3.

- [22] Jianhua Zhao et al. "Automated Autofluorescence Background Subtraction Algorithm for Biomedical Raman Spectroscopy". In: Applied Spectroscopy 61.11 (Nov. 2007), pp. 1225–1232. DOI: 10.1366/000370207782597003. URL: https://doi.org/10.1366/000370207782597003.
- [23] S. A. Maier et al. "Plasmonics-A Route to Nanoscale Optical Devices". In: Advanced Materials 13.19 (Sept. 2001), pp. 1501-1505. DOI: 10.1002/1521-4095(200110)13:19<1501::aid-adma1501>3.0.co;2-z. URL: https://doi.org/10.1002/1521-4095(200110)13:19%3C1501::aid-adma1501%3E3.0.co;2-z.
- [24] Stefan Enoch and Nicolas Bonod, eds. Plasmonics. en. 2012th ed. SPringer series in optical sciences. Berlin, Germany: Springer, July 2012.
- [25] Dmitri K. Gramotnev and Sergey I. Bozhevolnyi. "Plasmonics beyond the diffraction limit". In: Nature Photonics 4.2 (Feb. 2010), pp. 83-91. ISSN: 1749-4893. DOI: 10.1038/nphoton.2009.282. URL: https://doi.org/10.1038/nphoton.2009.282.
- [26] P.R. West et al. "Searching for better plasmonic materials". In: Laser & amp Photonics Reviews 4.6 (Mar. 2010), pp. 795–808. DOI: 10.1002/lpor.200900055. URL: https://doi.org/10.1002/lpor.200900055.
- [27] Yael Gutiérrez et al. "Plasmonics beyond noble metals: Exploiting phase and compositional changes for manipulating plasmonic performance". In: Journal of Applied Physics 128.8 (Aug. 2020), p. 080901. DOI: 10.1063/5.0020752. URL: https://doi.org/10.1063/5.0020752.
- [28] Alemayehu Nana Koya et al. "Nanoporous Metals: From Plasmonic Properties to Applications in Enhanced Spectroscopy and Photocatalysis". In: ACS Nano 15.4 (Apr. 2021), pp. 6038–6060. DOI: 10.1021/acsnano.0c10945. URL: https://doi.org/10.1021/acsnano.0c10945.
- [29] Gustav Mie. "Beiträge zur Optik trüber Medien, speziell kolloidaler Metallösungen". In: Annalen der Physik 330.3 (1908), pp. 377–445. DOI: 10.1002/andp.19083300302. URL: https://doi.org/10.1002/andp. 19083300302.
- [30] F. Papoff and B. Hourahine. "Geometrical Mie theory for resonances in nanoparticles of any shape". In: Opt. Express 19.22 (Oct. 2011), pp. 21432-21444. DOI: 10.1364/0E.19.021432. URL: http://opg.optica.org/oe/abstract.cfm?URI=oe-19-22-21432.
- [31] Mohammad Habibur Rahaman and Brandon Kemp. "Revisiting Mie's scattering theory for the analysis of the plasmonic resonance of metal nanospheres". In: *Journal of Electromagnetic Waves and Applications* 0 (Sept. 2016), pp. 1–11. DOI: 10.1080/09205071.2016.1231089.
- [32] Da-Shin Wang, Fu-Yin Hsu, and Chii-Wann Lin. "Surface plasmon effects on two photon luminescence of gold nanorods". In: Optics Express 17.14 (June 2009), p. 11350. DOI: 10.1364/oe.17.011350. URL: https://doi.org/10.1364/oe.17.011350.
- [33] Jan Becker et al. "The Optimal Aspect Ratio of Gold Nanorods for Plasmonic Bio-sensing". In: Plasmonics 5.2 (Mar. 2010), pp. 161–167. DOI: 10.1007/s11468-010-9130-2. URL: https://doi.org/10.1007/s11468-010-9130-2.
- [34] M Muldarisnur et al. "Size and aspect ratio dependency of sensitivity of ellipsoidal metal nanoparticle based liquid sensor". In: IOP Conference Series: Materials Science and Engineering 578.1 (Sept. 2019), p. 012035. DOI: 10.1088/1757-899x/578/1/012035. URL: https://doi.org/10.1088/1757-899x/578/1/012035.
- [35] Maxim Sukharev et al. "Optical properties of metal nanoparticles with no center of inversion symmetry: Observation of volume plasmons". In: Phys. Rev. B 76 (18 Nov. 2007), p. 184302. DOI: 10.1103/PhysRevB. 76.184302. URL: https://link.aps.org/doi/10.1103/PhysRevB.76.184302.
- [36] Jed Ziegler and Richard Haglund. "Plasmonic Response of Nanoscale Spirals". In: Nano letters 10 (Aug. 2010), pp. 3013–8. DOI: 10.1021/nl101475n.
- [37] A. Stewart, S. Murray, and S. E. J. Bell. "Simple preparation of positively charged silver nanoparticles for detection of anions by surface-enhanced Raman spectroscopy". In: The Analyst 140.9 (2015), pp. 2988–2994. DOI: 10.1039/c4an02305f. URL: https://doi.org/10.1039/c4an02305f.
- [38] Yuwei Pei et al. "Highly sensitive SERS-based immunoassay with simultaneous utilization of self-assembled substrates of gold nanostars and aggregates of gold nanostars". In: J. Mater. Chem. B 1 (32 2013), pp. 3992–3998. DOI: 10.1039/C3TB00519D. URL: http://dx.doi.org/10.1039/C3TB00519D.
- [39] Jacob Pettine et al. "Plasmonic nanostar photocathodes for optically-controlled directional currents". In: Nature Communications 11.1 (Mar. 2020). DOI: 10.1038/s41467-020-15115-0. URL: https://doi.org/10.1038/s41467-020-15115-0.
- [40] Arun Patel et al. "Gold nanoflowers as efficient hot-spots for surface enhanced Raman scattering". In: (Apr. 2016).
- [41] Sijia Yi et al. "One-step synthesis of dendritic gold nanoflowers with high surface-enhanced Raman scattering (SERS) properties". In: RSC Adv. 3 (26 2013), pp. 10139-10144. DOI: 10.1039/C3RA40716K. URL: http://dx.doi.org/10.1039/C3RA40716K.
- [42] Sebastian Thomas et al. "Large optical field enhancement for nanotips with large opening angles". In: (2014). DOI: 10.48550/ARXIV.1412.8172. URL: https://arxiv.org/abs/1412.8172.
- [43] Yong Wu et al. "Plasmonic near-field focusing with nanotips structure". In: International Symposium on Multispectral Image Processing and Pattern Recognition. 2018.
- [44] Rostislav Bukasov et al. "Probing the Plasmonic Near-Field of Gold Nanocrescent Antennas". In: ACS Nano 4.11 (Nov. 2010), pp. 6639–6650. DOI: 10.1021/nn101994t. URL: https://doi.org/10.1021/nn101994t.
- [45] Gerard Macias et al. "Surface roughness boosts the SERS performance of imprinted plasmonic architectures". In: J. Mater. Chem. C 4 (18 2016), pp. 3970–3975. DOI: 10.1039/C5TC02779A. URL: http://dx.doi.org/10.1039/C5TC02779A.

- [46] Qiangqiang Fu et al. "Rough surface Au@Ag core—shell nanoparticles to fabricating high sensitivity SERS immunochromatographic sensors". In: Journal of Nanobiotechnology 13.1 (Nov. 2015). DOI: 10.1186/s12951-015-0142-0. URL: https://doi.org/10.1186/s12951-015-0142-0.
- [47] Sijing Ding et al. "Surface-roughness-adjustable Au nanorods with strong plasmon absorption and abundant hotspots for improved SERS and photothermal performances". In: Nano Research 15.3 (Aug. 2021), pp. 2715– 2721. DOI: 10.1007/s12274-021-3740-1. URL: https://doi.org/10.1007/s12274-021-3740-1.
- [48] Feng Wang and Y R Shen. "General properties of local plasmons in metal nanostructures." In: Physical review letters 97 20 (2006), p. 206806.
- [49] V. G. Kravets et al. "Plasmonic Surface Lattice Resonances: A Review of Properties and Applications". In: Chemical Reviews 118.12 (June 2018), pp. 5912-5951. DOI: 10.1021/acs.chemrev.8b00243. URL: https://doi.org/10.1021/acs.chemrev.8b00243.
- [50] Frédéric Laux, Nicolas Bonod, and Davy Gérard. "Single Emitter Fluorescence Enhancement with Surface Lattice Resonances". In: The Journal of Physical Chemistry C 121.24 (June 2017), pp. 13280-13289. DOI: 10.1021/acs.jpcc.7b04207. URL: https://doi.org/10.1021/acs.jpcc.7b04207.
- [51] Charles Cherqui et al. "Plasmonic Surface Lattice Resonances: Theory and Computation". In: Accounts of Chemical Research 52.9 (Aug. 2019), pp. 2548-2558. DOI: 10.1021/acs.accounts.9b00312. URL: https://doi.org/10.1021/acs.accounts.9b00312.
- [52] Taerin Chung et al. "Plasmonic Nanostructures for Nano-Scale Bio-Sensing". In: Sensors (Basel, Switzerland) 11 (Dec. 2011), pp. 10907–29. DOI: 10.3390/s111110907.
- [53] Hong Wei et al. "Multipolar Plasmon Resonances in Individual Ag Nanorice". In: ACS Nano 4.5 (Apr. 2010), pp. 2649–2654. DOI: 10.1021/nn1002419. URL: https://doi.org/10.1021/nn1002419.
- [54] Michael B. Ross, Chad A. Mirkin, and George C. Schatz. "Optical Properties of One-, Two-, and Three-Dimensional Arrays of Plasmonic Nanostructures". In: Journal of Physical Chemistry C 120 (2016), pp. 816– 830.
- [55] Pablo Albella et al. "Low-loss electric and magnetic field-enhanced spectroscopy with subwavelength silicon dimers". In: *Journal of Physical Chemistry C* 117 (2013), pp. 13573–13584.
- [56] Kristina Frizyuk et al. "Enhancement of Raman scattering in dielectric nanostructures with electric and magnetic Mie resonances". In: *Physical Review B* 97 (2018), p. 085414.
- [57] Martín Caldarola et al. "Non-plasmonic nanoantennas for surface enhanced spectroscopies with ultra-low heat conversion". In: *Nature Communications* 6.1 (Aug. 2015), pp. 7915–13803. ISSN: 2041-1723. DOI: 10.1038/ncomms8915. URL: https://doi.org/10.1038/ncomms8915.
- [58] Saman Jahani and Zubin Jacob. "All-dielectric metamaterials". In: Nature Nanotechnology 11.1 (Jan. 2016), pp. 23–36. ISSN: 1748-3395. DOI: 10.1038/nnano.2015.304. URL: https://doi.org/10.1038/nnano.2015.304.
- [59] Reuben M. Bakker et al. "Magnetic and Electric Hotspots with Silicon Nanodimers". In: Nano Letters 15.3 (Feb. 2015), pp. 2137-2142. DOI: 10.1021/acs.nanolett.5b00128. URL: https://doi.org/10.1021/acs.nanolett.5b00128.
- [60] M. Kerker, D.-S. Wang, and C. L. Giles. "Electromagnetic scattering by magnetic spheres". In: J. Opt. Soc. Am. 73.6 (June 1983), pp. 765-767. DOI: 10.1364/JOSA.73.000765. URL: http://opg.optica.org/abstract.cfm?URI=josa-73-6-765.
- [61] Ivano Alessandri and John R Lombardi. "Enhanced Raman Scattering with Dielectrics." In: Chemical reviews 116 24 (2016), pp. 14921–14981.
- [62] Siyka I. Shopova et al. "Plasmonic enhancement of a whispering-gallery-mode biosensor for single nanoparticle detection". In: Applied Physics Letters 98 (2011), p. 243104.
- [63] Subhendu Chandra and Joydeep Chowdhury. "SERS on all dielectric materials: A brief review". In: 28 (July 2019), pp. 177–189.
- [64] Raymond C Rumpf. Advanced electromagnetics: 21th century electromagnetics. Lecture 1 concept of Diffraction From Gratings. Sept. 2022.
- [65] Howard Devoe. "Optical Properties of Molecular Aggregates. I. Classical Model of Electronic Absorption and Refraction". In: *Journal of Chemical Physics* 41 (1964), pp. 393–400.
- [66] M.A. Yurkin and A.G. Hoekstra. "The discrete dipole approximation: An overview and recent developments". In: Journal of Quantitative Spectroscopy and Radiative Transfer 106.1 (2007). IX Conference on Electromagnetic and Light Scattering by Non-Spherical Particles, pp. 558-589. ISSN: 0022-4073. DOI: https://doi.org/10.1016/j.jqsrt.2007.01.034. URL: https://www.sciencedirect.com/science/article/pii/S0022407307000556.
- [67] Edward M. Purcell and Carlton R. Pennypacker. "Scattering and Absorption of Light by Nonspherical Dielectric Grains". In: The Astrophysical Journal 186 (1973), pp. 705–714.
- [68] Keith T. Carron et al. "Resonances of two-dimensional particle gratings in surface-enhanced Raman scattering". In: Journal of The Optical Society of America B-optical Physics 3 (1986), pp. 430–440.
- [69] Patrick C. Chaumet, A. Rahmani, and Garnett W. Bryant. "Generalization of the Coupled Dipole Method to Periodic Structures". In: *Physical Review B* 67 (2003), p. 165404.
- [70] Shengli Zou and George C. Schatz. "Narrow plasmonic/photonic extinction and scattering line shapes for one and two dimensional silver nanoparticle arrays". In: The Journal of Chemical Physics 121.24 (2004), p. 12606. DOI: 10.1063/1.1826036. URL: https://doi.org/10.1063/1.1826036.

- [71] Alastair D. Humphrey and William L. Barnes. "Plasmonic surface lattice resonances on arrays of different lattice symmetry". In: *Physical Review B* 90.7 (Aug. 2014). DOI: 10.1103/physrevb.90.075404. URL: https://doi.org/10.1103/physrevb.90.075404.
- [72] Baptiste Auguié and William L. Barnes. "Collective Resonances in Gold Nanoparticle Arrays". In: Physical Review Letters 101.14 (Sept. 2008). DOI: 10.1103/physrevlett.101.143902. URL: https://doi.org/10. 1103/physrevlett.101.143902.
- [73] Vadim A. Markel and Andery K. Sarychev. "Surface plasmons in ordered and disordered chains of metal nanospheres". In: 2007 Quantum Electronics and Laser Science Conference (2007), pp. 1–2.
- [74] Baptiste Auguié and William L. Barnes. "Diffractive coupling in gold nanoparticle arrays and the effect of disorder". In: Opt. Lett. 34.4 (Feb. 2009), pp. 401-403. DOI: 10.1364/OL.34.000401. URL: http://opg. optica.org/ol/abstract.cfm?URI=ol-34-4-401.
- [75] Gabriel A. Vecchi, Vincenzo Giannini, and Jaime Gómez Rivas. "Surface modes in plasmonic crystals induced by diffractive coupling of nanoantennas". In: *Physical Review B* 80 (2009), pp. 1–4.
- [76] Eric C. Le Ru, Pablo G. Etchegoin, and Matthias Meyer. "Enhancement factor distribution around a single surface-enhanced Raman scattering hot spot and its relation to single molecule detection." In: The Journal of chemical physics 125 20 (2006), p. 204701.
- [77] Andrea R. Tao et al. "Langmuir-Blodgett Silver Nanowire Monolayers for Molecular Sensing Using Surface-Enhanced Raman Spectroscopy". In: Nano Letters 3 (2003), pp. 1229–1233.
- [78] Shemaiah M Weekes et al. "Macroscopic arrays of magnetic nanostructures from self-assembled nanosphere templates." In: Langmuir: the ACS journal of surfaces and colloids 23 3 (2007), pp. 1057–60.
- [79] Ling Zhang et al. "Wrinkled nanoporous gold films with ultrahigh surface-enhanced Raman scattering enhancement." In: ACS nano 5 6 (2011), pp. 4407–13.
- [80] Peng Mao et al. "Broadband single molecule SERS detection designed by warped optical spaces". In: *Nature Communications* 9 (2018).
- [81] Thakshila Liyanage et al. "Fabrication of a self-assembled and flexible SERS nanosensor for explosive detection at parts-per-quadrillion levels from fingerprints." In: The Analyst 143 9 (2018), pp. 2012–2022.
- [82] Chang Chen et al. "High spatial resolution nanoslit SERS for single-molecule nucleobase sensing". In: *Nature Communications* 9 (2018).
- [83] Jian-An Huang et al. "SERS discrimination of single DNA bases in single oligonucleotides by electroplasmonic trapping". In: *Nature Communications* 10 (2019).
- [84] Javier Cambiasso et al. "Surface-Enhanced Spectroscopies of a Molecular Monolayer in an All-Dielectric Nanoantenna". In: ACS Photonics 5.4 (Apr. 2018), pp. 1546-1557. DOI: 10.1021/acsphotonics.7b01604. URL: https://doi.org/10.1021/acsphotonics.7b01604.
- [85] Xianyu Ao. "Surface mode with large field enhancement in dielectric-dimer-on-mirror structures". In: Opt. Lett. 43.5 (Mar. 2018), pp. 1091-1094. DOI: 10.1364/OL.43.001091. URL: http://opg.optica.org/ol/abstract.cfm?URI=ol-43-5-1091.
- [86] Syed K. Islam et al. "Surface-Enhanced Raman Scattering on a Chemically Etched ZnSe Surface". In: The Journal of Physical Chemistry C 117.44 (Nov. 2013), pp. 23372–23377. ISSN: 1932-7447. DOI: 10.1021/jp407647f. URL: https://doi.org/10.1021/jp407647f.
- [87] Syed K. Islam and John R. Lombardi. "Enhancement of surface phonon modes in the Raman spectrum of ZnSe nanoparticles on adsorption of 4-mercaptopyridine". In: The Journal of Chemical Physics 140.7 (Feb. 2014), p. 074701. DOI: 10.1063/1.4865136. URL: https://doi.org/10.1063/1.4865136.
- [88] Richard Livingstone et al. "Surface Enhanced Raman Spectroscopy of Pyridine on CdSe/ZnBeSe Quantum Dots Grown by Molecular Beam Epitaxy". In: *The Journal of Physical Chemistry C* 114.41 (Oct. 2010), pp. 17460–17464. ISSN: 1932-7447. DOI: 10.1021/jp105619m. URL: https://doi.org/10.1021/jp105619m.
- [89] Dmitry Maznichenko, Krishnan Venkatakrishnan, and Bo Tan. "Stimulating Multiple SERS Mechanisms by a Nanofibrous Three-Dimensional Network Structure of Titanium Dioxide (TiO2)". In: *The Journal of Physical Chemistry C* 117.1 (Jan. 2013), pp. 578–583. ISSN: 1932-7447. DOI: 10.1021/jp310193a. URL: https://doi.org/10.1021/jp310193a.
- [90] Xiaoqi Fu et al. "Surface-enhanced Raman scattering of 4-mercaptopyridine on sub-monolayers of α-Fe2O3 nanocrystals (sphere, spindle, cube)". In: Journal of Raman Spectroscopy 40 (2009), pp. 1290–1295.
- [91] Yanfei Wang et al. "Direct observation of surface-enhanced Raman scattering in ZnO nanocrystals". In: Journal of Raman Spectroscopy 40 (2009), pp. 1072–1077.
- [92] Pu Liu et al. "Fabrication of Si/Au Core/Shell Nanoplasmonic Structures with Ultrasensitive Surface-Enhanced Raman Scattering for Monolayer Molecule Detection". In: The Journal of Physical Chemistry C 119.2 (Jan. 2015), pp. 1234–1246. ISSN: 1932-7447. DOI: 10.1021/jp5111482. URL: https://doi.org/10. 1021/jp5111482.
- [93] Chen-Chi Huang et al. "3D Ag/ZnO hybrids for sensitive surface-enhanced Raman scattering detection". In: Applied Surface Science 365 (2016), pp. 291–295.
- [94] Zong-Hong Lin and Huan-Tsung Chang. "Preparation of Gold-Tellurium Hybrid Nanomaterials for Surface-Enhanced Raman Spectroscopy". In: Langmuir 24.2 (Dec. 2007), pp. 365–367. DOI: 10.1021/la702543k. URL: https://doi.org/10.1021/la702543k.
- [95] Xiangxin Xue et al. "Surface-enhanced Raman scattering of molecules adsorbed on Co-doped ZnO nanoparticles". In: Journal of Raman Spectroscopy 43.1 (May 2011), pp. 61–64. DOI: 10.1002/jrs.2988. URL: https://doi.org/10.1002/jrs.2988.

- [96] Libin Yang, Xin Jiang, and Ming Yang. "Improvement of surface-enhanced Raman scattering performance for broad band gap semiconductor nanomaterial (TiOsub2/sub): Strategy of metal doping". In: Applied Physics Letters 99.11 (Sept. 2011), p. 111114. DOI: 10.1063/1.3638467. URL: https://doi.org/10.1063/1.3638467.
- [97] Xiao Xia Han et al. "Semiconductor-enhanced Raman scattering: active nanomaterials and applications". In: Nanoscale 9 (15 2017), pp. 4847-4861. DOI: 10.1039/C6NR08693D. URL: http://dx.doi.org/10.1039/C6NR08693D.
- [98] Qiuming Yu et al. "Inverted size-dependence of surface-enhanced Raman scattering on gold nanohole and nanodisk arrays." In: *Nano letters* 8 7 (2008), pp. 1923–8.
- [99] Daniela Lospinoso et al. "Self-Assembled Metal Nanohole Arrays with Tunable Plasmonic Properties for SERS Single-Molecule Detection". In: Nanomaterials 12.3 (2022). ISSN: 2079-4991. DOI: 10.3390/nano12030380. URL: https://www.mdpi.com/2079-4991/12/3/380.
- [100] Carlos Escobedo. "On-chip nanohole array based sensing: a review". In: Lab Chip 13 (13 2013), pp. 2445—2463. DOI: 10.1039/C3LC50107H. URL: http://dx.doi.org/10.1039/C3LC50107H.
- [101] Kane Yee. "Numerical solution of initial boundary value problems involving maxwell's equations in isotropic media". In: IEEE Transactions on Antennas and Propagation 14.3 (1966), pp. 302–307. DOI: 10.1109/TAP. 1966.1138693.
- [102] URL: https://optics.ansys.com/hc/en-us/articles/360034914633-Finite-Difference-Time-Domain-FDTD-solver-introduction.
- [103] T. B. (Thomas Byron) Jones. Electromechanics of particles. eng. Cambridge; Cambridge University Press, 1995. ISBN: 0521431964.
- [104] Deb Shankar Ray. Notes on Brownian motion and related phenomena. 1999. arXiv: physics/9903033 [physics.ed-ph].
- [105] Zhe Xu, Wuzhou Song, and Kenneth B. Crozier. "Optical Trapping of Nanoparticles Using All-Silicon Nanoantennas". In: ACS Photonics 5.12 (Nov. 2018), pp. 4993-5001. DOI: 10.1021/acsphotonics.8b01250. URL: https://doi.org/10.1021/acsphotonics.8b01250.
- [106] Partha Pratim Patra et al. "Plasmofluidic single-molecule surface-enhanced Raman scattering from dynamic assembly of plasmonic nanoparticles". In: Nature Communications 5.1 (July 2014). DOI: 10.1038/ncomms5357. URL: https://doi.org/10.1038/ncomms5357.
- [107] Weihua Zhang et al. "Trapping and Sensing 10 nm Metal Nanoparticles Using Plasmonic Dipole Antennas".
 In: Nano Letters 10.3 (Feb. 2010), pp. 1006–1011. DOI: 10.1021/nl904168f. URL: https://doi.org/10.1021/nl904168f.
- [108] Mathieu L. Juan, Maurizio Righini, and Romain Quidant. "Plasmon nano-optical tweezers". In: Nature Photonics 5.6 (June 2011), pp. 349-356. ISSN: 1749-4893. DOI: 10.1038/nphoton.2011.56. URL: https://doi.org/10.1038/nphoton.2011.56.
- [109] Maurizio Righini, Anna S. Zelenina, and Romain Quidant. "Parallel and selective trapping in a patterned plasmonic landscape". In: 2007 IEEE/LEOS International Conference on Optical MEMS and Nanophotonics (2007), pp. 61–62.
- [110] Changjun Min et al. "Focused plasmonic trapping of metallic particles". In: Nature Communications 4.1 (Dec. 2013), p. 2891. ISSN: 2041-1723. DOI: 10.1038/ncomms3891. URL: https://doi.org/10.1038/ncomms3891.
- [111] Sarp Kerman et al. "Raman fingerprinting of single dielectric nanoparticles in plasmonic nanopores". In: Nanoscale 7 (44 2015), pp. 18612-18618. DOI: 10.1039/C5NR05341B. URL: http://dx.doi.org/10.1039/C5NR05341B.
- [112] Pietro Strobbia, Adam Mayer, and Brian M Cullum. "Improving Sensitivity and Reproducibility of SERS Sensing in Microenvironments Using Individual, Optically Trapped Surface-Enhanced Raman Spectroscopy(SERS) Probes". In: Appl. Spectrosc. 71.2 (Feb. 2017), pp. 279-287. URL: http://opg.optica.org/as/abstract.cfm?URI=as-71-2-279.
- [113] Ansys Lumerical Inc. Lumerical FDTD. Version R1.1. July 28, 2022. URL: https://optics.ansys.com/.
- [114] COMSOL. COMSOL Multiphysics. Version 6.0 U2. Nov. 30, 2022. URL: https://www.comsol.com/.

Appendices

Ouerv

A Literature research

The previous work done at TNO by [15] and [16] served as an introduction to the field during the orientation phase of the literature review and several of their most relevant references were used in the literature review. Afterwards Scopus was used to find other relevant papers. Sorting was set to "cited by most" in order to prioritize influential papers. Depending on the relevancy to the research questions the search results were assessed by looking first at the title and abstract. Subsequently, if relevant enough the article was quickly read/skimmed to confirm relevancy and sorted according to topic. In fig 30 a table can be found of the used search terms. Another part of the literature was collected through references of prior found literature. It must be noted that plasmonics was not excluded because certain design aspects are analogous with dielectric SERS. Three books were additionally read in order to increase basic understanding of principles and concepts within the field. Many chapters of "Modern electrodynamics" by Zangwill, The first three chapters of "Raman spectroscopy for chemical analysis" by McReery and the first five chapter of "Plasmonics: From Basics to Advanced Topics" by Enoch and Bonod.

Documents

Query	Documents
TITLE-ABS-KEY (metal-free AND sers)	45
TITLE-ABS-KEY (all-dielectric AND sers)	18
TITLE-ABS-KEY (trapping W/4 sers)	62
TITLE-ABS-KEY ("circular polarization" sers)	11
TITLE-ABS-KEY (silicon W/4 sers)	232
TITLE-ABS-KEY (morphology AND dependent AND resonance W/4 pla smonic)	22
TITLE-ABS-KEY (morphology AND dependent AND resonance W/4 die lectric)	43
TITLE-ABS-KEY (surface AND lattice AND resonance W/4 plasmonic)	214
TITLE-ABS-KEY (surface AND lattice AND resonance W/4 dielectric)	35
TITLE-ABS-KEY (semiconductor W/4 sers)	206
TITLE-ABS-KEY (dielectric W/4 sers)	79

Figure 30: List of used search terms extracted from Scopus. Left the search query used and right the number of articles found.

B Convergence test

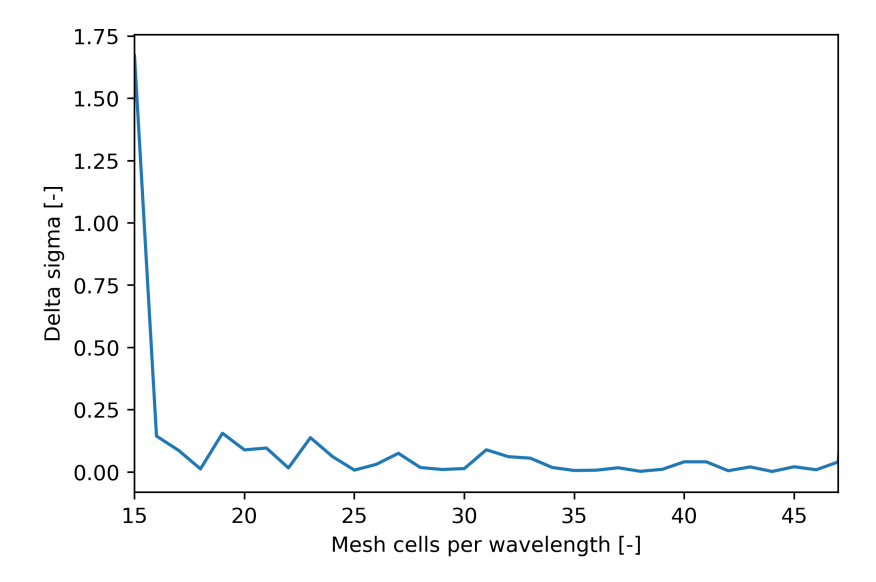


Figure 31: Convergence of the Cameron metasurface design for EF against the number of mesh cells per wavelength in Lumerical

C Reproduction Cameron

The COMSOL simulations in [16] were accessible the fineness of the meshing could be easily modified. In COMSOL the mesh setting tab has 8 levels were coarse is the 5th and finer is the 3th finest option. In fig 32 these two levels are plotted against each other to show how the simulation of Kenworthy was not at a point were the meshing had converged. The excitation resonance is approximately 33% lower and the raman shift enhancement at several places a few percent. Given that the average volume EF depends on the square of the excitation resonance this result in more than 55% lower value for the average volume EF. Another COSMOL file contained two frequency points calculated with extremely fine meshing, the finest option in COMSOL, for the wavelengths 785 nm and 850 nm and correspond to the values found in 32.

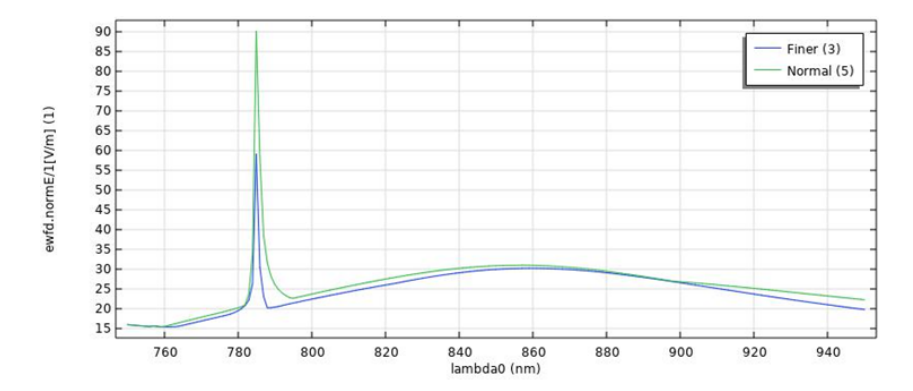


Figure 32: Graph created from original Kenworthy et al. COMSOL simulation with meshing parameter normal and rerun simulation with meshing parameter finer [16].

D Lumerical settings

In the table the lumerical settings and some fixed variables are given. Some default settings of Lumerical version 2022~R2.4 are excluded. Settings are different for sweeps and final simulations, and linear and circular polarization are also included.

Setting tab	setting/value				
General simulation region					
Simulation time	15000 fs				
Simulation Temperature	300 K				
Background material	H2O (water) Hale and Querry				
Mesh Refinement	Conformal variant 1				
Mesh cells per wavelength	sweeps: 20 final: 50				
z max	sweeps: top cylinder $+$ 850nm final: top spacer $+$ 1183nm				
PML					
PML type	Stretched coordinate PML				
PML Profile	Steep angle				
PML layers	32				
allow symmetry on all boundaries	linear pol: yes circular pol: no				
x min bc	linear pol: Anti-symmetric circular pol: periodic				
x max bc	linear pol: Anti-symmetric circular pol: n/a				
y min bc	linear pol: Symmetric circular pol: periodic				
y max bc	linear pol: Symmetric circular pol: n/a				
z min bc	PML				
z max bc	PML				
Extend structure through pml	yes				
Source					
Source shape	Plane wave				
Amplitude	linear pol: 1 circular pol: both sources $1/\sqrt{2}$				
Phase (degrees)	linear pol: 0 circular pol: source1 at 0 and source2 at 90				
polarization angle (degrees)	linear pol: 0 circular pol: source1 at 0 and source2 at 90				
Plane wave type	bloch/periodic				
Injection axis	z-axis				
Direction	backward				
Z max	z max simulation region minus 10nm				
Wavelength start	$750\mathrm{nm}$				
Wavelength stop	950.56nm				
Gold slab					
Material	Au (Gold) Johnson and Christy				
Z span	100nm				
Spacer					
Material	SiO2 (Fused silica) Malitson				
Z span	10nm				
Cylindrical nano particles					
material	Si (silicon) Vuye				

E Additional results multiple structures

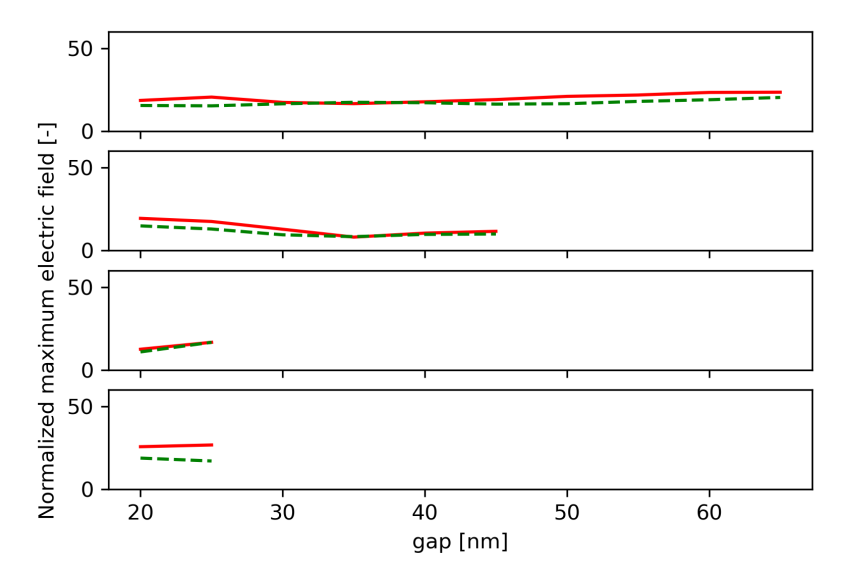


Figure 33: Normalized ME vs gap found during exploration of metasurfaces. Red solid line: linear polarization. Green dashed line circular polarization. top pentamer, upper middle hexamer, lower middle heptamer, lower octamer.

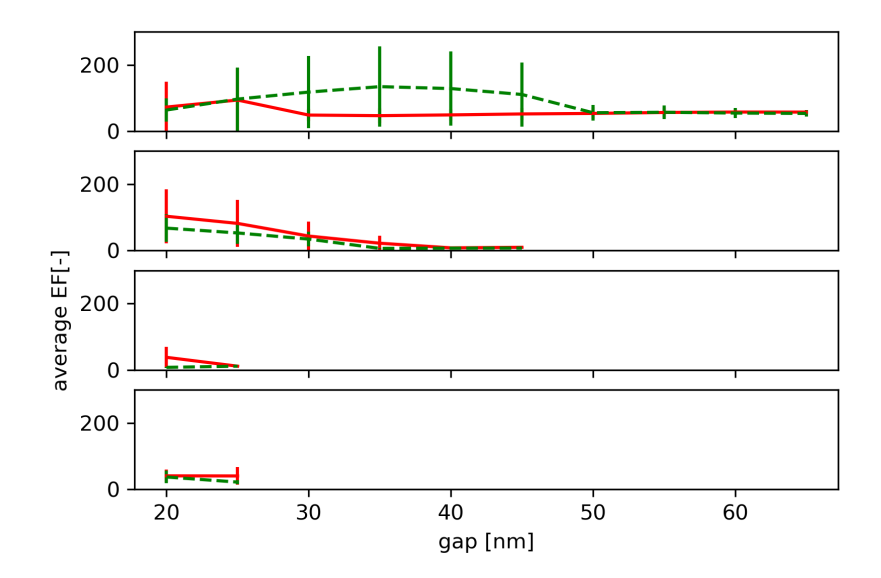


Figure 34: Average EF vs gap found during exploration of metasurfaces. Red solid line: linear polarization. Green dashed line circular polarization. top pentamer, upper middle hexamer, lower middle heptamer, lower octamer.

F Variable structure parameters metasurfaces

Table of all variable structure paramaters for all metasurface designs. The units of all variables is in nanometers except for the ratios which are dimensionless.

Metasurface	Height	Diameter	X unit cell	Y unit cell	${f Height/gap}$	${f Height/diameter}$
Dimer 20 nm	564.4	123.0	556.0	556.0	28.22	4.59
Dimer 130 nm	900.0	98.0	556.0	556.0	6.92	9.19
Quadrumer 20 nm	315.0	99.0	556.0	556.0	15.75	2.65
Quadrumer 60 nm	640.0	96.0	556.0	556.0	10.67	6.67
Quadrumer 130 nm	680.0	76.0	556.0	556.0	5.23	8.95
Line 60 nm	780.0	122.0	81.0	500.0	13	6.35

G Comparison of trapping distributions between various metasurfaces

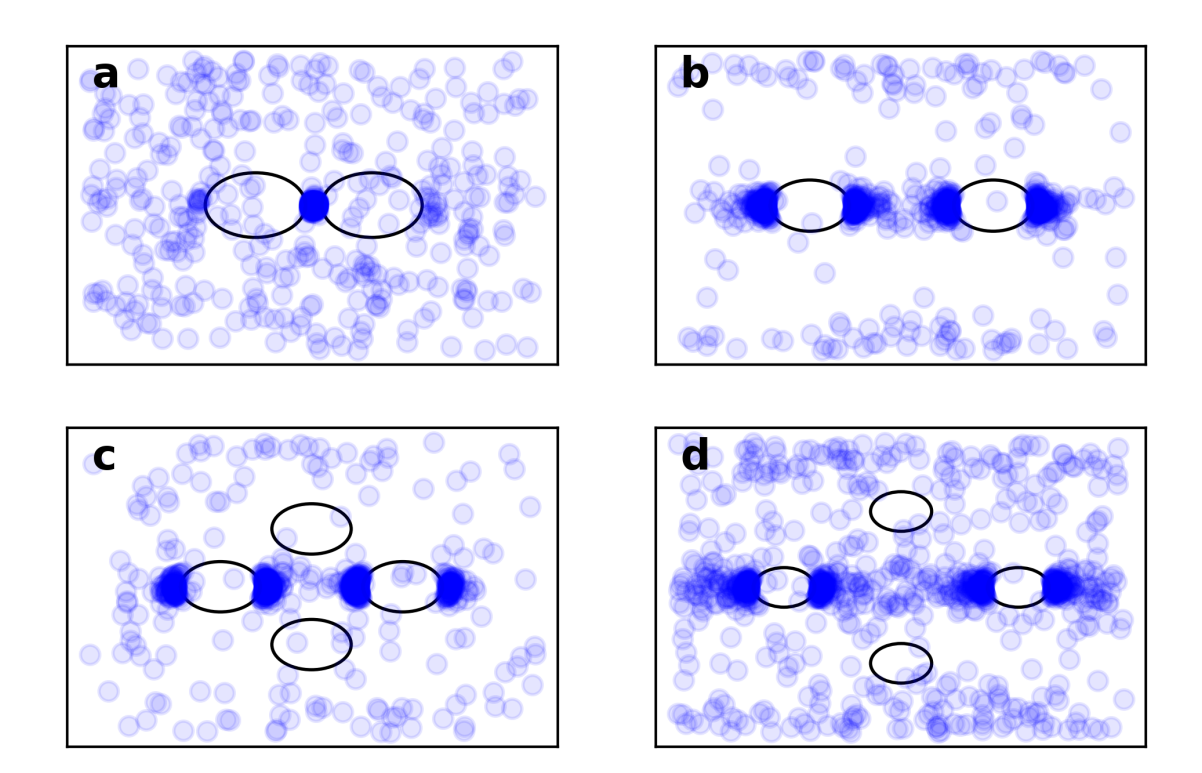


Figure 35: x-y distributions in the free volume after optical trapping of particles with diameter 10 nm for dimer and quadrumer metasurfaces excited with linear polarization. All unit cells of the quadrumers have x-y dimensions of 556 nm by 556 nm. The blue semi-transpart circles give the end positions of the particles. a: 20 nm dimer. b: 130 nm dimer. c: 60 nm quadrumer. d: 130 nm quadrumer.

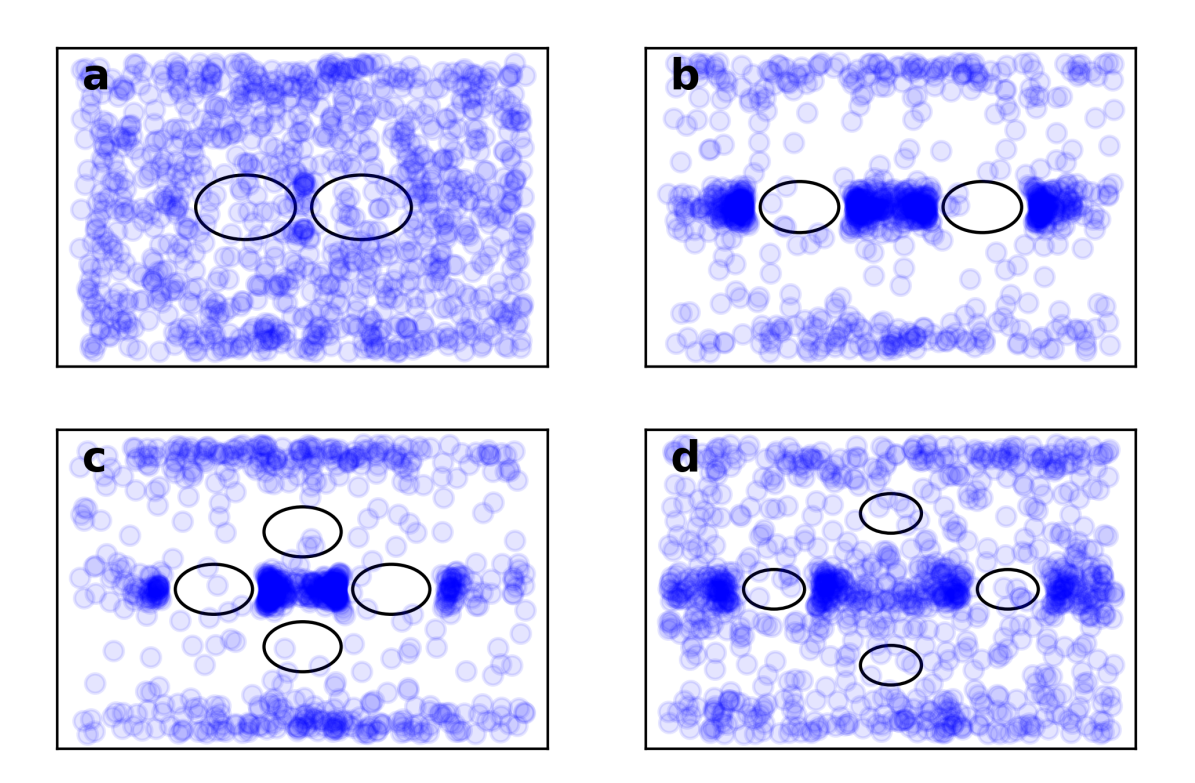


Figure 36: x-y distributions in the free volume after optical trapping of particles with diameter 40 nm for dimer and quadrumer metasurfaces excited with linear polarization. All unit cells of the quadrumers have x-y dimensions of 556 nm by 556 nm. The blue semi-transpart circles give the end positions of the particles. a: 20 nm dimer. b: 130 nm dimer. c: 60 nm quadrumer. d: 130 nm quadrumer.

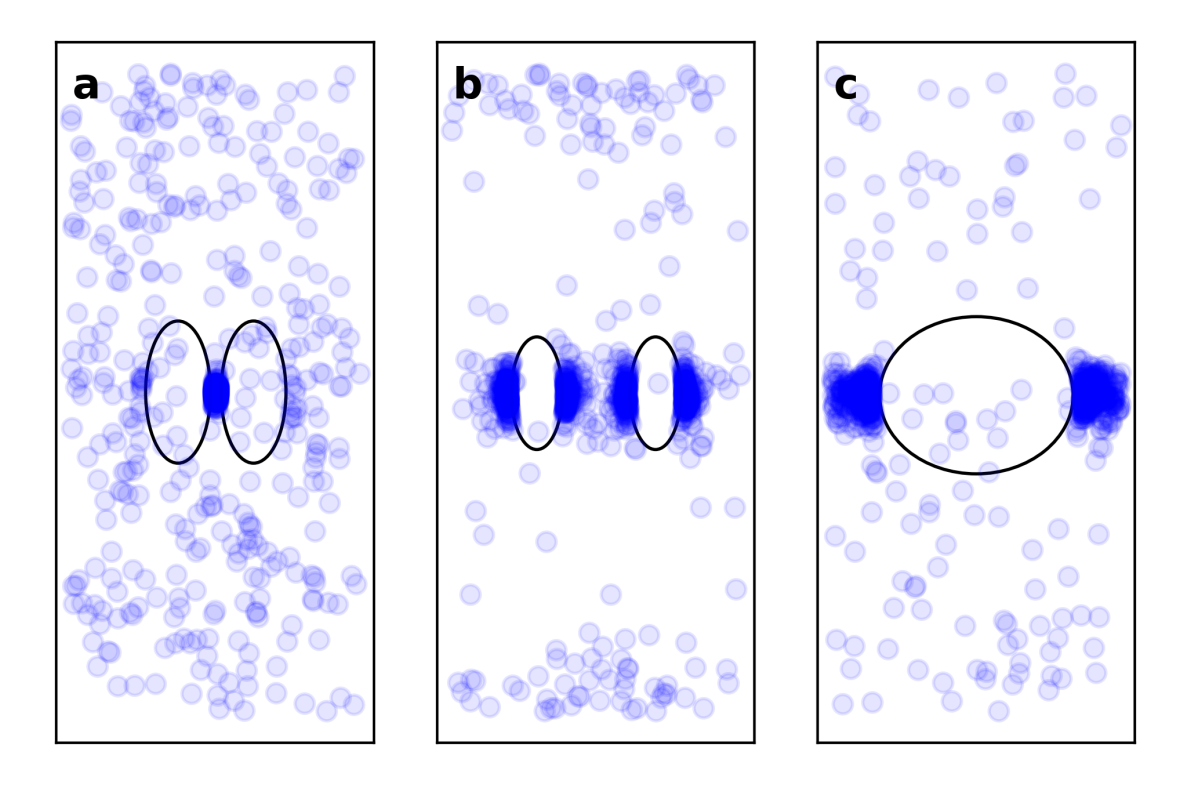


Figure 37: x-y distributions in the free volume after optical trapping of particles with diameter 10 nm for different metasurfaces excited with linear polarization. The dimensions of the unitcell are given as indicated in appendix F. The blue semi-transpart circles gives the end positions of the particles. $\bf a$: 20 nm dimer. $\bf b$: 130 nm dimer. $\bf c$: 60 nm line